Doctoral Dissertation (Censored)

博士論文 (要約)

A study on coupling processes between cumulus convection and atmospheric disturbances based on analyses of equatorial Rossby and Kelvin waves

(赤道 Rossby 波と赤道 Kelvin 波の解析に基づく積雲対流と大気擾乱との結合過程に関する研究)

A Dissertation Submitted for the Degree of Doctor of Philosophy
December 2021

令和３年 12 月 博士（理学）申請

Department of Earth and Planetary Science, Graduate School of Science,
The University of Tokyo

東京大学大学院理学系研究科

地球惑星科学専攻

Yuhi Nakamura

中村 雄飛

Abstract

Coupling processes between moist cumulus convection and large-scale atmospheric environments are essential to determine large-scale global circulations. However, our understanding is still limited, and climate model simulations do not capture this coupling processes. In this study, we quantitatively investigate the coupling processes based on the convectively coupled equatorial waves (CCEWs), which are major coupled disturbances in the tropics. Previous studies theoretically suggested coupling mechanisms, and they are recently categorized into two groups; the gravity wave mode which focuses on a connection between the gravity wave structure and convective activity and the moisture mode which constructs disturbances of the column water vapor (CWV) including feedback with precipitation. However, it has not been clarified yet how the coupling mechanisms work on the actual processes of the CCEWs. In this study, we investigate the details of convective couplings of equatorial Rossby and Kelvin waves which are considered to have contrasting nature in terms of the coupling processes. Furthermore, we aim to quantitatively investigate how convective activity drives and/or maintains wave disturbances. An accumulation of satellite observations newly enables us to directly quantify 3-dimensional precipitation characteristics, convective heating, and radiative heating. The eddy energy budget analysis can be improved by more realistic estimation of heating profiles. We also aim to make a suggestion on the commonality of the equivalent depths among various CCEW modes based on statistical analyses.

The theoretical backgrounds and observational contributions from previous studies are summarized in the introduction, Chapter 1. The datasets which are utilized in this study are described in Chapter 2. The analyses methods of wave phase determination, definition of rainfall events, and

composite analyses are also described.

We utilize the products of the Tropical Rainfall Measuring Mission (TRMM) precipitation radar (PR) observation. The TRMM observation produces 3-dimensional distribution of precipitation, which directly captures detailed characteristics of rainfall event. Convective heating profiles are retrieved based on the 3-dimensional precipitation data. Furthermore, this provides long-term and consistent observation for 14 years, and thus this dataset is advantageous on statistical analyses. We further utilize CloudSat and CALIPSO satellite data, which provide properties of cloud and radiation. The statistical analyses enable us to estimate combining convective heating from TRMM to radiative heating from CloudSat/CALIPSO.

In Chapter 3, the dynamical and thermodynamical structures of convectively coupled Rossby and Kelvin waves are investigated. The purpose of this Chapter is to quantitatively discuss the existence of theoretically suggested coupling mechanisms in the observed coupled waves. The gravity wave mode can be tested through the phase relationships between vertical motion and temperature, and the moisture mode is discussed based on amplitudes of CWV and their phase relationships to precipitation. Furthermore, convective heating profiles estimated from TRMM are used in order to reliably quantify the eddy energy budget. The satellite-derived heating profiles have not been applied yet to the eddy energy budget analysis.

First, we clarified that the Rossby waves can be assigned to the moisture mode and Kelvin waves correspond to the gravity wave mode. The phase relationship between anomalous vertical motion and temperature is in phase for the Rossby waves and is nearly in quadrature for the Kelvin waves. This strongly suggests the Kelvin waves as the gravity wave mode. Furthermore, it is quantified that the amplitude of CWV is larger in the Rossby wave composite by one-order than in the Kelvin wave composite. Especially, the negative CWV anomaly is nearly zero in the Kelvin waves. The Rossby waves can be amplified and maintained through a feedback process from precipitation anomaly which is in phase with the CWV anomaly. The Rossby waves can be assigned into the moisture mode group in terms of the characteristics of CWV fluctuation. Second, we further quantify the eddy energy budget and found that both waves are driven by top-heavy convective heating, even though they can be assigned to different coupling modes. We also detected that the vertical distributions of the eddy available potential energy (EAPE) generation terms and conversion terms from EAPE to eddy kinetic energy are similar. This may approach the similarity of their equivalent depths.

In Chapter 4, the detailed evolutions of rainfall events utilizing TRMM PR dataset are investigated. The 3-dimensional precipitation radar observation quantitatively clarifies the detailed precipitation characteristics coupled with the Rossby waves or the Kelvin waves, which cannot be directly investigated with objective analyses. We define rainfall events and their 3 indices to express precipitation characteristics utilizing 3-dimensional TRMM PR observation and classify the rainfall events into 5 types: mesoscale convective system (MCS), deep convection, congestus convection, shallow convection, and others. The type of others can be interpreted as stratiform anvil rain in a decaying MCS. We clarify the detailed evolutions of convective activity, which have not been shown in previous studies.

For the Rossby wave composite, the MCS and deep convective events are simultaneously activated, while in the later period of convectively suppressed phase, the shallow and congestus convective events frequently occur. On the other hand, for the Kelvin wave composite, a distinct 5-type evolution from the shallow convective events to the decaying MCS is revealed. We also found that the MCSs dominate in precipitation amount for both waves, and thus the top-heavy heating, which corresponds to the vertical profiles of EAPE shown in Chapter 3, can be induced by these MCS events.

In Chapter 5, the cloud and radiative heating properties are investigated based on CloudSat and CALIPSO observations. These satellites products provide new observational profiles of radiative heating, while radiation and its contribution on diabatic heating has been hardly estimated before. The long-term statistics along the wave phase in this study provides consistent results between precipitation and cloud characteristics. The estimations of diabatic heating associated with the Rossby and the Kelvin waves are achieved for the first time, by combining the convective heating from TRMM and radiative heating from CloudSat and CALIPSO.

We quantified the net effect of radiative heating, which is positive in EAPE generation for both waves. The EAPE generation increases by considering the radiative heating by 30% for the Rossby waves, and by 42% for the Kelvin waves. The upper anvil cloud and the middle-level stratiform cloud deck are almost in phase in the Rossby wave composite. On the other hand, the upper anvil cloud precedes the stratiform cloud deck in the Kelvin wave composite. We found that this difference modulates the role of radiative heating, especially for the longwave radiation. In the Rossby wave composite, shortwave radiation can amplify the EAPE generation, although longwave radiation reduces the EAPE generation. On the other hand, in the Kelvin wave composite, both shortwave and longwave radiation play a role to amplify the EAPE generation.

A general conclusion is presented in Chapter 6. Similarities between the Rossby waves and the Kelvin waves are found as large contributions by MCSs for precipitation amount and a dominance of top-heavy heating on the EAPE generation, and the radiative heating can enhance this EAPE generation in both waves, whereas the coupling processes and the evolutions of precipitation characteristics are different. This similarity may approach the similar values of the equivalent depths among the convectively coupled equatorial wave modes. The slight upward shift of the peak of heating profile due to radiation seen in the Kelvin waves may correspond to a slight difference in the equivalent depth indicated in the zonal-time spectrum. The vertical profiles of diabatic heating may approach the definition process of the equivalent depths.

Analyses in this study are expected to be applied to other equatorial wave modes and the MJO in order to reveal and compare details of various coupling disturbances, and a theoretical approach is required as a future work to shed light on determination processes of equivalent depths of CCEWs based on the diabatic heating.

Contents

Chapter 1.

General Introduction

1.1. Motivations on studying convectively coupled disturbances in the tropics

Atmospheric disturbances coupled with moist convection have been observed in the tropics in various spatiotemporal scales: inertia gravity waves in a few days, synoptic wave disturbances in several days or a few weeks, and intraseasonal oscillations. On the other hand, cumulus convection in the tropics also plays an essential role in global circulations of moisture and energy. Interactions with cumulus convection, which typically indicate a lifetime of a few or several hours, are essential for these coupled synoptic disturbances. Wave disturbances modulate environmental conditions for cumulus convection and an ensemble of cumulus convection supplies diabatic heating as an energy source of disturbances. Despite of this basic idea, various mechanisms have been suggested, but not have led to a consensus yet, and numerous numbers of global climate models have still been struggling to reproduce realistic behaviors of convectively coupled disturbances. On the other hand, notable selectivity of phase speeds and spatiotemporal scales of these convectively coupled disturbances has also been observed. Each kind of coupled disturbances has its own specific scale. However, at this point, a theoretical foundation to explain this selectivity is not satisfactory.

Here, we aim to clarify detailed profiles of coupled disturbances to improve our knowledge about the coupling mechanisms. An accumulation of satellite observations has an ability to bring about new findings on evolutions of convective activity and associated diabatic heating, while it is difficult for numerical models to explicitly or sufficiently represent those phenomena. In this Chapter, findings and suggestions from previous studies are summarized in the followings, and our goals are presented.

1.2. Equatorial Waves and its convective coupling

A complete set of wave solutions in tropical region were theoretically derived by Matsuno (1966) for the hydrostatic equation with equatorial β-plane. Their dispersion curves correspond to inertia gravity wave, Rossby wave, Kelvin wave, and mixed Rossby-gravity wave. On the other hand, some observational studies found wave disturbances in the upper troposphere and the lower stratosphere. Yanai and Maruyama (1966) detected the westward-propagating disturbances whose period is about 5 days and phase speed is 23 m/s in the lower equatorial stratosphere. Wallace and Kousky (1968) also found an eastward-propagating disturbance whose period is about 15 days and phase speed is around 10 m/s in the lower equatorial stratosphere. These findings are observational evidence for the mixed Rossby-gravity waves and the Kelvin waves, respectively. These multiple wave modes are called as the equatorial waves. Their phase speeds are related to the equivalent depth which is a constant determined from the vertical structure of atmospheric stratification. It is an important parameter to understand the wave characteristics.

As for the tropospheric waves, Liebmann and Hendon (1990) showed the existence of a disturbance near the international date line with a period of 4–5 days had a mixed Rossby-gravity wave structure. Takayabu and Nitta (1993) showed their differences from the easterly waves, which had been intensively studied in the tropical meteorology field, by Yanai and Murakami (1970) and Reed et al. (1977), for example. Takayabu (1994), using the infrared brightness temperature data, found that the spatiotemporal spectrum of cloud activity shows a dispersion pattern that corresponds to equatorial wave modes, with a significantly slower phase speed compared to that of free waves calculated from the tropospheric stratification. Wheeler and Kiladis (1999) also confirmed this feature by applying a red-noise filter to the power spectral analysis on outgoing longwave radiation (OLR). The above studies indicated a common equivalent depth among various equatorial wave modes which are relatively shallow compared to what is expected from dry theory (cf. Salby and Garcia 1987).

These waves are known as convectively coupled equatorial waves (CCEWs) and their comprehensive review is provided by Kiladis et al. (2009).

1.3. Moist convection in the tropics

Moist convection in the tropics plays an important role on global circulations of moisture and energy. Since this subgrid-scale phenomenon could not be treated explicitly in conventional numerical models, convective parameterizations have been developed (e.g., Arakawa and Schubert 1974; Betts and Miller 1986). However, climate model simulations have been struggling with uncertainties of precipitation and cloud processes (e.g., Stevens and Bony 2013). To improve our understanding on relationships between convective activity and circulations, and to contribute to improvements of convective parameterization, massive field observational campaigns have been held: the Global Atmospheric Research Program's (GARP) Atlantic Tropical Experiment (GATE) in the summer 1974, and the Tropical Ocean–Global Atmosphere Coupled Ocean Atmosphere Response Experiment (TOGA COARE) from November 1992 to February 1993, for example.

Among them, a tri-modal nature of cumulus development was detected in the TOGA COARE observation, consisting of shallow convection, congestus convection, and deep convection (Johnson et al. 1999). Each type of convection corresponds to stable layers in the typical tropical atmosphere; the trade inversion, the melting layer, and the tropopause, respectively. Moreover, the deep convection is often organized with stratiform precipitation, which is characterized by a bright band signal of radar observation. This organized convection with stratiform precipitation is referred as a mesoscale convective system (MCS).

Previous studies showed an importance of column or free tropospheric water vapor. In tropical oceanic regions, precipitation amounts exponentially increase with the column water vapor (CWV) amount (Bretherton et al. 2004; Peters and Neelin 2006). Brown and Zhang (1997) and Yoneyama and

Fujitani (1995) found the reduction of deeply developed convection when the free troposphere is dry using TOGA COARE sounding. Numaguti et al. (1995) also showed the similar reduction of deep convection with a dry air intrusion, and further discussed moisture modifications from wave disturbances. More recently, Takayabu et al. (2010) showed that shallow and congestus convection are sensitive to sea surface temperature (SST), while deep convection is clearly suppressed when the free troposphere is subsiding and dry, even over high SST, utilizing space-borne radar observation.

An importance of a deep development of a convective tower has been focused on, as a subsequent issue to CWV. Kumar et al. (2013) showed that the large-scale dynamics prepared middle-level moisture and helped deeper development of shallow convection. Holloway and Neelin (2009), Hirota et al. (2011) and Schiro and Neelin (2019) investigated the entrainment effect on a convective parcel and speculated that dry free troposphere can disrupt its buoyancy. According to these perspectives, the CWV may be important for maintaining the buoyancy of a convective plume through its entrainment processes. On the other hand, Ahmed and Schumacher (2015) indicated that the rapid increase of precipitation to CWV is achieved mainly by a large extension of stratiform precipitation belonging to MCSs. The squall line system, which is a kind of MCS, was investigated by Zipser (1977) using aircraft observation, and by Houze (1977) based on the GATE radar observation. As Bryan and Fritsch (2000) extended the static stability with the moist absolute instability, the MCS is characterized by a mesoscale layer lifting circulation (Rutledge 1991; Moncrieff 1992; Mechem et al. 2002). These studies showed that the importance of free tropospheric humidity on deep development of convection, or organized MCS in different ways.

The tendencies of the column saturation fraction and precipitation over the tropical ocean showed cyclical coevolution around an attractor across a wide spatiotemporal scale (Wolding et al. 2020a). The detrainment processes or moisture transport by shallow or congestus convection can form positive feedback called as moisture-convection feedback (Grabowski and Moncrieff 2004). Interactions between convective activity and synoptic scale moisture field is an essential issue in the tropical meteorology.

A methodology to diagnose bulk properties of convection in a synoptic condition was also developed. Yanai et al. (1973) defined the apparent heat source Q_1 as latent heating with radiative heating plus eddy convergence of dry static energy s, and the apparent moisture sink Q_2 as condensation plus eddy divergence of moisture:

$$Q_1 = \frac{\partial \bar{s}}{\partial t} + \overline{\nabla \cdot s\boldsymbol{v}} + \frac{\partial \bar{s}\bar{\omega}}{\partial p} = Q_R + L(c-e) - \frac{\partial}{\partial p}\overline{s'\omega'}, \tag{1.1}$$

$$Q_2 = -L\left(\frac{\partial \bar{q}}{\partial t} + \overline{\nabla \cdot q\boldsymbol{v}} + \frac{\partial \bar{q}\bar{\omega}}{\partial p}\right) = L(c-e) + L\frac{\partial}{\partial p}\overline{q'\omega'}. \tag{1.2}$$

The overbars denote the large-scale horizontal means, which is expected to be an order of 100 km, and primes denote convective scale eddies. The c and e are condensation and evaporation, respectively. The L is latent heat of evaporation. Different types of convection, such as tri-modal nature and stratiform precipitation, show different vertical profiles of diabatic heating. The shallow and congestus convection indicate positive heating below 5km height. The deep convection indicates positive heating in almost all troposphere with its peak around 5-6 km height. This heating profile is referred to as "bottom-heavy heating". On the other hand, the stratiform precipitation indicate positive heating in upper troposphere and negative heating in lower troposphere due to evaporation of rain droplets. The heating profile of MCSs is represented by combining that of deep convection and stratiform precipitation. When the ratio of stratiform precipitation in a MCS increases, the peak of positive heating shifts upward and typically locates around 8 km height (Houze 1989). This heating profile of MCSs is referred to as "top-heavy heating". These heating profiles are schematically depicted in preceding studies (cf. Schumacher et al. 2004; Khouider and Majda 2006). In these schematics, the deep convection is assigned to the first baroclinic mode, and the congestus convection and stratiform precipitation is assigned to the second baroclinic mode with opposite signs.

Recently, space-borne precipitation radar observations opened up the possibilities to reveal the nature of convective activity globally and statistically. Takayabu (2002) summarized vertical distributions of precipitation using Tropical Rainfall Measuring Mission (TRMM) precipitation radar (PR) observation. A series of study by Shige et al. (2004, 2007, 2008, 2009) developed the algorithm for estimation of vertical distributions of Q_1, Q_2, and latent heating based on TRMM observation. Takayabu et al. (2010) revealed the relationship among convective activity, its heating profiles, and environmental conditions in different types of convection.

1.4. Convective coupling of tropical disturbances

Convectively coupled equatorial waves (CCEWs), TD-type disturbances (cf. Takayabu and Nitta 1993; Lau and Lau 1990), and the Madden-Julian Oscillation (MJO; Madden and Julian 1971) are the major moist disturbances in the tropics. Not only their dynamical circulations but also characteristics of coupled convection are important. Utilizing TOGA-COARE field campaign observations, and infrared observations from the geostationary satellite, Takayabu et al. (1996) showed a lifecycle convection associated with the quasi 2-day wave, which corresponds to convectively coupled inertia gravity waves. The convection showed an evolution as shallow, congestus convection, deep convective towers, mature stratiform precipitation, and a decaying phase. Convectively coupled Kelvin wave shows a similar schematic lifecycle (Straub and Kiladis 2003a). Kikuchi and Takayabu (2004) further found a similar evolution of cumulus convection in the MJO, observed from the geostationary satellite as well as radio sonde observations from the TOGA-COARE field campaign. Mapes et al. (2006) featured the similarities of lifecycles of these evolutions among various temporal and spatial scales ranging from individual MCSs to the MJO and called it as a “self-similarity”.

As the satellite observation data is accumulated, statistical analyses became more effective to capture characteristics of convective activity. Lubis and Jacobi (2015) quantified contribution to the climatology of precipitation amount which is attributed to CCEWs. Yasunaga and Mapes (2012a,b) performed cross spectrum analyses between CWV and precipitation amount and speculated that divergent waves tend to couple with MCS, and rotational waves tend to couple with isolated convection. Furthermore, Wolding et al. (2020b) have shown proportions of precipitation diagnosed from the column saturation fraction based on Bretherton et al. (2004). Rossby waves and MJO indicated large fraction of 80% and almost 100% of successful diagnosis from the column saturation fraction, respectively. On the other hand, Kelvin waves showed only 50%. Furthermore, Roundy and Frank (2004) indicated an absence of a spectrum peak of CWV corresponding to Kelvin waves, despite existence of spectrum peaks of OLR. These studies suggested that connections between CWV and precipitation are different among equatorial wave modes and MJO. Rossby waves and MJO more tightly connect to CWV than Kelvin waves. This connection is important in the context of the coupling mechanisms.

1.5. Suggested coupling mechanisms

Idealized simple models suggested various coupling mechanisms. Recently, convectively coupled disturbances were divided into two groups based on the ratio of adjustment timescales between moist convection and temperature perturbation: gravity wave mode and moisture mode (e.g., Adames et al. 2019; Adames and Maloney 2021). Adames et al. (2019) suggested that Kelvin waves and inertia gravity waves are assigned to the gravity wave mode, and Rossby waves and MJO are assigned to the moisture mode.

The gravity wave mode is originally constructed upon the instability of the second kind connected to convection, which is called as wave-CISK (cf. Yamasaki 1969; Hayashi 1970; Lindzen 1974). This instability assumes a high correlation between lower horizontal convergence and diabatic heating due to convective activity. Under this assumption, the gravity waves with the first baroclinic mode and Kelvin waves with vertically tilted structure can be amplified by synchronized upper warm anomaly and diabatic heating. Although this assumed correlation is generally seen in the tropics, the wave-CISK is not valid for explaining its time and spatial scales. For example, Matthews and Lander (1999) showed that the smallest scale disturbances in a numerical grid are most unstable with the wave-CISK. On the other hand, a simple model using convective parameterization controlled by convective inhibition yielded larger spatiotemporal scale disturbances known as a stratiform instability (Mapes 2000). The first and second baroclinic modes are associated with convective and stratiform modes, respectively. These two vertical normal modes allow a simple model to represent organized convective systems, which is ubiquitously observed in the tropics (Johnson et al. 1999; Houze 1989). Furthermore, combining these modes with mid-level moisture (Kuang 2008) yielded a tri-modal convective evolution as follows: shallow convection, deep convection, and organized systems with stratiform rain. This is referred to as a moisture-stratiform instability. Previous numerical model research also clearly showed an unstable mode with a front-to-rear vertical tilt, corresponding to the gravity wave mode. This tilted unstable mode produced a stage of pre-conditioning by shallow convection, a mature stage with deep convection, and a later stage with stratiform rain (Khouider and Majda 2006, 2007, 2008) and the amplification by top-heavy diabatic heating with upper warm anomaly of vertically tilted structure (Tulich et al. 2007).

In contrast with the gravity wave mode, which is primarily dynamically driven, Neelin and Yu (1994) derived another unstable mode based on the moist convective adjustment and a scaling by a typical lifetime of convection. Sobel et al. (2001) derived a moisture wave that balances with the background moisture gradient under a weak temperature gradient condition. This unstable mode is now referred to as a moisture mode. The theoretical framework of this mode was constructed by many previous studies (Fuchs and Raymond 2002, 2005, 2007; Sugiyama 2009a,b; Sobel and Maloney 2012; Raymond et al. 2015), and has been applied in the context of the MJO (Sobel and Maloney 2013; Adames and Kim 2016) and convectively coupled equatorial Rossby waves recently (Fuchs-

Stone et al. 2019). Actually in the tropics, precipitation amounts exponentially increase as the column saturation fraction increases (Bretherton et al. 2004; Peters and Neelin 2006). Thus, this moisture mode introduces an aspect of connection between the synoptic moisture field modification and the convective activity.

Raymond and Fuchs (2007) constructed a simple idealized model employing a convective parametrization, which has a part connected to the convective inhibition or buoyancy and another part connected to the CWV. This model realized contrasting two unstable modes. The first one has a vertically tilted structure, and its precipitation corresponds to the buoyancy part of convective parameterization. The second one has a vertically erect structure with slow propagation, and its precipitation depends on the CWV part of convective parameterization. It is an important suggestion that whether the vertical structure is tilted or erect can correspond to which part of convective parameterization is associated with. Furthermore, both contrasted unstable modes are activated in one simple model. This finding may approach a coupling mechanism of various convectively coupled disturbances.

However, global climate numerical models struggle to reproduce realistic CCEWs and MJO. Lin et al. (2006) investigated detailed reproducibility of CCEWs and their variance among a large number of climate model simulations used for Intergovernmental Panel on Climate Change (IPCC) Fourth Assessment Report (AR4). Each climate model produces some time-space spectrum signals of CCEWs but often with faster phase speeds, or deeper equivalent depths. In a certain model, the reproducibility severely varies depending on equatorial wave modes. Furthermore, focusing on a certain wave mode, the reproducibility also severely varies among climate models. These huge variances can be resulted from the fact that different models employ different convective parameterizations. Lin et al. (2008) further investigated impacts of convective parameterization scheme on reproducibility of CCEWs. Suzuki et al. (2006) showed that CCEWs, except for Rossby waves, vanish when convective parameterization is modulated to eliminate sensitivity to middle-level moisture. These studies suggested that CCEWs' reproducibility highly depends on convective parameterizations and can be tested for the model performances.

1.6. The objectives of this study

The first objective of this study is to quantitatively investigate the coupling mechanisms of the actual waves. Observational and statistical studies showed CCEWs' structures (section 1.2) and coupled convective activity (section 1.3), and studies using idealized simple models suggested coupling mechanisms (section 1.4). We need to rethink validity of suggested coupling mechanisms and their works on processes of the CCEWs in the real world. Here, a comparative study is useful because of the contrasting nature between convective couplings of equatorial Rossby and Kelvin waves. In Chapter 3, we quantitatively investigate how the contrast of structures of Rossby and Kelvin waves correlate with the moisture mode and the gravity wave mode. Furthermore, we aim to quantitatively investigate and discuss how these coupling mechanisms are achieved through the eddy energy budget, utilizing convective heating estimations from TRMM observational products. Applying the satellite-derived convective heating to the eddy energy budget is a new attempt.

Secondary, we aim to clarify detailed precipitation characteristics, and cloud and radiative properties associated with CCEWs, utilizing multiple satellite observations, and to quantify the radiative heating in order to estimate total diabatic heating. In general, convective activity and cloud properties are difficult to estimate in numerical models and reanalysis data because we should be careful about their resolutions and biases. Observational data products by space-borne radar and lidar enable us to deal with precipitation and cloud characteristics. However, gridded products called Level 3 data, which are mainly used by previous studies referred in section 1.3, are not favorable for detailed studies precipitation characteristics, without of 3-dimensional radar signals obtained in Level 2 or orbital data. We perform long-term and quantitative statistics with the TRMM PR orbital (Level 2) products to directly reveal detailed precipitation characteristics in Chapter 4, and with CloudSat and CALIPSO orbital products to investigate cloud properties and its radiative effect associated with Rossby and Kelvin waves in Chapter 5. These approaches are expected to more directly capture detailed precipitation characteristics and cloud properties. Furthermore, we aim to estimate the apparent heat source Q_1 associated with the CCEWs with combining use of convective heating and radiative heating.

At last, the commonality of equivalent depths among CCEWs is a significant unresolved issue. Recently, idealized models produced disturbances corresponding to some modes of CCEWs with realistic phase speeds, or equivalent depths (e.g., Khouider and Majda 2008). However, a problem on parameter tuning still remains, and theoretical background has not been constructed yet. We aim to seek a determination factor of the equivalent depth based on statistical analyses of convectively coupled disturbances and detailed precipitation and cloud properties. The commonality will be discussed at the point of observed phenomena.

Chapter 2.

Data and Methodology

2.1. Data description

Datasets are used in the period from December 2001 to November 2014 for reanalysis dataset ERA5, TRMM PR and SLH, SSM/I, and OISST, and from June 2006 to August 2010 for CloudSat and CALIPSO.

2.1.1. merged IR dataset

We used a long-term consistent brightness temperature (T_b) data, which is Cloud Archive User Service (CLAUS) dataset (Hodges et al. 2000) along with a globally merged infrared radiation dataset provided by NOAA/NCEP (Janowiak et al. 2001). The source of CLAUS dataset is thermal infra-red radiances from International Satellite Cloud Climatology Project (ISCCP). The detailed merging procedure and its validity are described in Dias et al. (2017). The horizontal grid resolution is 0.5° and the temporal resolution is 3 hours.

2.1.2. ERA5, reanalysis dataset

We utilize ERA5, reanalysis dataset, which produced by European Centre for Medium-Range Weather Forecasts (ECMWF) (Hersbach et al. 2020). Variables used in this study are as follows: 3-dimensional wind, temperature, specific humidity, geopotential, and model calculations of fluxes of surface sensible and latent heat, and radiation at the top of atmosphere and at the surface. The ERA5 dataset, which has originally 0.25° horizontal grid and 1-hourly temporal resolution, is converted to 0.5° horizontal grid and employed with 3-hourly temporal resolution to match with that of T_b data.

2.1.3. TRMM PR and rainfall event dataset

The Tropical Rainfall Measuring Mission (TRMM) is a satellite which observed tropical precipitation. It is launched on November 1997 and re-entered Earth's atmosphere on June 2015. During its operation, TRMM experienced its altitude change on August 2001, and there is a gap of data quality after this change (cf. Short and Nakamura 2010). We utilize the data after this altitude change. TRMM employed the Low Earth orbit with its observation range from 35°S to 35°N, and thus the satellite passed a certain location at different local time.

The precipitation radar (PR) on TRMM have its frequency of Ku-band (13.796 and 13.802 GHz), which is favor of tropical rainfall. The swath width of TRMM PR is 220 km. Its horizontal resolution around the surface is about 5 km, and its vertical resolution is 250 m. The minimum threshold of TRMM PR reflectivity for detection of echo top in each observational ray is 17 dBZ, which corresponds to about 0.5 mm/hr of near the surface precipitation.

The 2A23 produces the rain type flags using PR observation. The rain flag, which partitions radar observation into convective rain, stratiform rain, and others (Awaka et al. 1997, 2007), is defined on each observational ray. This partitioning is based on vertical profile and horizontal distribution of radar reflectivity. For example, a bright band pattern corresponds to stratiform precipitation (Awaka et al. 2009). The shallow rain is also detected as warm rain under the level of 0°C temperature. The storm top is defined as the highest level where radar beam detects precipitative droplet.

The 2A25 product provides vertical profiles of radar reflectivity with correction of rain attenuation and retrieves precipitation amount based on the Z-R relationships (Iguchi and Meneghini 1994; Iguchi et al. 2000). The vertical distribution and near surface precipitation amount are estimated.

The products of version 7 are used. This is the latest version developed for TRMM observation. We should note that recent versions are developed for Global Precipitation Measurement (GPM) and applied to TRMM consistently. We define rainfall event dataset on the orbital observation by TRMM three-dimensional PR using estimated precipitation amount in 2A25 and the rain flag classification in 2A23. The detailed procedure is described in later section.

2.1.4. TRMM spectral latent heating (SLH)

The 2H25 product estimates latent heating, convective heating $Q_1 - Q_R$ and apparent moisture sink Q_2 of Yanai et al. (1973). This product is called spectral latent heating (SLH; Shige et al. 2004, 2007, 2008, 2009; Takayabu and Tao 2020). This product is based on the spectral representation of vertical distributions of precipitation which is classified by its top height in an observational ray and its rain flag defined in 2A23 product (cf. Takayabu 2002), and the heating profiles are calculated with the two-dimensional Goddard Cumulus Ensemble model (Tao and Simpson 1993; Tao 2003; Tao et al. 2003). The vertical resolution is 1 km interval except for the lowest layer with 500 m interval. The version 7 product is also used.

2.1.5. SSM/I dataset

The Special Sensor Microwave Imager (SSM/I) is a satellite of passive microwave imager. The dataset (Meissner and Wentz 2012; Wentz 2013) provides ocean measurements including surface wind speed, atmospheric column water vapor (CWV), Cloud Liquid Water, and Rain Rate. Here we utilized CWV and surface wind speed. This dataset provides gridded data with 0.25° horizontal resolution, and we regrid it to 0.5° to match the grid interval of T_b in section 2.1.1. The temporal resolution is once a day with time of data acquisition.

2.1.6. Optimum Interpolation Sea Surface Temperature

The Optimum Interpolation Sea Surface Temperature (OISST) dataset (Reynolds et al. 2007;

Huang et al. 2021) is employed to analyze sea surface temperature (SST) when the Rossby and Kelvin waves pass through. This provides daily mean SST with 0.25° grid interval, which is retrieved by satellite data from the Advanced Very High Resolution Radiometer and Advanced Microwave Scanning Radiometer. Its grid interval is converted into 0.5° to match with that of T_b.

2.1.7. CloudSat and CALIPSO

The CloudSat and Cloud-Aerosol Lidar and Infrared Pathfinder Satellite Observation (CALIPSO) are satellites which are designed to observe vertical profiles of clouds. They participated the satellite constellation named A-train from April 2006 to February 2018, and they now compose C-train. These two satellites employ the sun-synchronous orbit, and thus crosses the equator twice a day at around 1:30 pm (ascending orbit) and 1:30 am (descending orbit) of local time.

The CloudSat has cloud profiling radar (CPR) whose frequency is 94 GHz and horizontal resolution is 1.4 km, and the CALIPSO has Cloud-Aerosol Lidar with Orthogonal Polarization (CALIOP). These CPR and CALIOP have curtain-shaped observational rays without its swing to perpendicular direction of the orbit. Thus, their data products are 2-dimensional: traveling direction and height. We use two data products, 2B-GEOPROF-LIDAR and 2B-FLXHR-LIDAR, which combine CPR and CALIOP observations. The thin cloud is better detected with including CALIOP to CPR observation.

The cloud fraction is defined as a ratio of hydrometeor content in an observational volume. Marchand et al. (2008) designed the estimation algorithm of the cloud fraction and provided 2B-GEOPROF product with vertical resolution of 480 m. The lidar observation from CALIOP (Mace et al. 2009) is merged onto 2B-GEOPROF and produced the 2B-GEOPROF-LIDAR product (Mace and Zhang 2014) with vertical resolution of 240 m. The cloud fraction in the 2B-GEOPROF-LIDAR product is utilized in the present study.

The 2B-FLXHR-LIDAR product (L'Ecuyer et al. 2008; Henderson et al. 2013) is used to estimate radiative heating. The radiative flux in this product is calculated based on the rain and cloud droplet properties obtained by products of CPR and CALIPSO observation, for example, 2B-CWC-RO and 2C-ICE, and MODIS observation as auxiliary data, with vertical distributions of temperature and moisture provided by reanalysis dataset provided by ECMWF. The radiative heating rate is defined by the convergence of this radiative flux. Its vertical resolution is 250 m interval. We should note that shortwave radiation does not exist in descending orbits because of midnight observation.

The products of version R05 is used. Only orbits, where both 2B-GEOPROF-LIDAR and 2B-FLXHR-LIDAR products are defined, are used in the present analyses.

2.2. Methodology

2.2.1. Wave phase determination

Spectrum analysis is performed on the symmetric part of T_b to detect Rossby and Kelvin waves and define its wave phase. Detailed procedures are described below.

A meridional running mean with overlapping windows of its width of 3° is applied to T_b, and then it is separated into symmetric and anti-symmetric parts to the equator. The Fast Fourier Transformation (FFT) is performed on 96-day segments of T_b, and zonal-time spectrum of the symmetric part of T_b is calculated (cf. Hayashi 1971). The filtering bands of zonal wavenumber, period, and dispersion curve to define signals of Rossby and Kelvin waves are shown in Table 2.1. We choose reference latitudes as 10°N for Rossby waves and the equator for Kelvin waves to focus on latitudes where variances of filtered T_b are zonally and climatologically large. Figure 2.1 shows the variances of the filtered T_b, and Fig. 2.2 shows spectra of the symmetric T_b at the reference latitude. The power spectra are divided by their red-noise as in Wheeler and Kiladis (1999).

Next, we define the wave phase from $-\pi$ to π based on the time-zonal filtered T_b at the reference latitude globally and annually. The local minimum of the filtered T_b beyond -1σ is assigned to the most convectively active point, and on the other hand the local maximum point beyond $+1\sigma$ is assigned to the most convectively inactive point. Here, the σ denotes the standard deviation of filtered T_b. For Kelvin waves, the active point is set to phase $-\pi/2$ and the inactive point is set to phase $\pi/2$, but for Rossby waves the active point is set to phase $\pi/2$ and the inactive point is set to phase $-\pi/2$. This means that the following figures retain the actual west-to-east direction. Therefore, Rossby waves propagate leftward and Kelvin waves propagate rightward, so that phase 0 corresponds to a phase with an increasing convective activity. We define the wave phase as the arcsine value of the filtered T_b normalized by its nearest peak value. Figure 2.3 shows an example of filtered T_b and locations of phase $\pm\pi/2$. In this definition, one wavelength corresponds to a length from $-\pi$ to π. Zonal and monthly histograms of the number of convectively active points are shown in Fig. 2.4. The Rossby wave occurrence is higher from December to May and lower from July to October (Fig. 2.4a). Its zonal variability is relatively smaller than seasonal variability. The Kelvin wave occurrence is remarkably higher in MAM and lower over the eastern Pacific Ocean and the Atlantic Ocean from June to October (Fig. 2.4b). The activity of convectively coupled Kelvin waves is known as strongly controlled by climatological variations of the sea surface temperature (Yang et al. 2003).

We also calculate the autocorrelation of the filtered T_b. The time and distance at which autocorrelation reaches zero are summarized in Table 2.1. This corresponds to 1/4 wavelength.

In general, the infrared T_b emphasizes upper tropospheric perturbations. Thus, results might be different when another variable which emphasizes lower tropospheric perturbations is used for the filtering. Since Yasunaga and Mapes (2012a) showed that precipitation and low-level horizontal divergences are well coherent, it is inferred that the essential results will be retained when low-level wind is used for wave filtering for example, while there may be a phase shift especially in the definition of phases $\pm\pi/2$.

2.2.2. Rainfall event dataset

We define a dataset of rainfall event, which is a contiguous area of pixels with surface precipitation amounts greater than 0.5 mm/hr, using the TRMM PR Level 2 data products of 2A23, 2A25, and 2H25. The details of these products are described in the former sections. Each rainfall event contains information of its location, date and time, sum of surface precipitation obtained from 2A25 product, and vertical profiles of total convective heating and apparent moisture sink ($Q_1 - Q_R$ and Q_2, Yanai et al. 1973) estimated in 2H25 product. The pixel which has the maximum surface precipitation amount in a rainfall event represents the event's date, time and location.

We define three indices to represent the precipitation characteristics of each rainfall event. The first index is the number of rainfall pixels (5 km × 5 km) of TRMM PR and is expressed in a dB value. This index represents the area of a rainfall event. A rainfall event with 20 dB pixel occupies 2,500 km^2 area, approximately 50km × 50km, for example. A smaller-size event implies an isolated convection, and a larger-size event implies a widely extension of stratiform cloud deck. The second index is the maximum echo top height in a rainfall event, which is produced in the 2A25 data product. The minimum threshold of TRMM PR reflectivity for detection of echo top in each observational ray is 17 dBZ. This index represents how tall the rain droplet reaches. When all values of echo top height in a rainfall event are undefined in the original product, that event is excluded from statistics. The third index is the stratiform precipitation ratio (SPR), or a ratio of stratiform precipitation amount to all precipitation amount in a rainfall-event. We refer to the precipitation flag, which is distinguish convective rain or stratiform rain and is defined on each pixel of radar observation in 2A23 data product (Awaka et al. 1997). A rainfall event with a higher SPR than 40% tends to be an organized convective system, whereas an event with a lower SPR tends to be more isolated-type convection.

We classified rainfall events into following 5 types to more directly capture evolutions of convective activity: MCS, deep convective event, congestus convective event, shallow convective event, and others. The MCS is defined as a rainfall event which has larger size than 10,000 km^2, taller echo top than 8 km, and higher SPR than 40%. Convective events with lower SPRs than 40% are divided into 3 types as follows. The deep convective event is defined as a rainfall event which has taller maximum echo top than 8 km. The congestus convective event has 4-8 km of maximum echo top, and the shallow convective event has lower maximum echo top than 4 km. These thresholds of maximum echo tops refer to Johnson et al. (1999). They showed that the melting level at 4.5 km in the tropics and the trade inversion layer at 2 km can be partitions of cumulus development. Since rain droplets appear to be blown up higher than these layers in radar observation, we choose 8 km and 4 km levels as thresholds of the classification. Some rainfall events that do not fit into any of the former 4 types are designated into the type of others. The mean vertical profiles of convective heating, $Q_1 - Q_R$ (cf. Yanai et al. 1973), of each type are shown in Fig. 2.5 to validate this classification. The top-heavy heating profile with its peak around 7 km height is confirmed in the MCS type, as expected from Houze (1982), for example. The convective events can be classified into three types with different height of the peaks of the convective heating, such as 5, 3, and 1.5 km height, and these types correspond to deep convection, congestus convection, and shallow convection, respectively. Takayabu (2002) summarized the vertical distributions of precipitation at different echo tops, and Takayabu et al. (2010) showed vertical profiles of convective heating of shallow or deep rain. This separated heating profiles are consistent to these previous studies, and thus this classification of convective events can be justified. The type of others indicates upper-level heating and almost zero heating below 5 km. This heating profile implies that rainfall events that is composed of stratiform anvil rain due to decaying MCS are assigned into the type of others. In Chapter 4, histograms with this classification are shown in Fig. 4.6 and a further discussion is made.

2.2.3. Composite analyses

We conduct composite analyses of synoptic scale disturbances using variables of ERA5, precipitation characteristics using rainfall event dataset of TRMM PR, and cloud and radiative properties using CloudSat and CALIPSO observations. The number of data points employed in composite analyses are summarized in Fig. 2.6. Downwardly convex distributions from $-\pi$ to 0 and from 0 to π are shown for almost all lines in Fig. 2.6. This is because the definition of wave phase based on the arcsine value of filtered T_b and linear binning of wave phase axes. Additionally, sharp peaks at $\pm\pi/2$ in Fig. 2.6a, b are caused by explicit assigning local minimum and maximum to those phases. The procedures of composite analyses are described below.

For all variables of ERA5, the time and zonal components of each data point are assigned to wave phase relative to filtered T_b space. Thus, for the composite field, the x-axis is the wave phase, and the y-axis and z-axis are the latitude and pressure coordinates, respectively. To eliminate annual and seasonal change, we use anomalous values from each year's 3-month seasonal average: DJF, MAM, JJA, and SON. Since the spatiotemporal resolution of ERA5 is notably smaller than that of CCEWs, we should restrict the degree of freedom for Student's *t*-test. Here we conduct a non-zero Student's *t*-test on the anomalous composite whose degree of freedom is the number of composited points divided by the grid number in autocorrelation spatial scale (Table 2.1). This composite of ERA5 is mainly used in Chapter 3.

Variables of SSM/I and SST obtained by OISST are composited in the same manner as ERA5 variables, except for the temporal resolution. The data point of SSM/I is assigned to 3-hourly wave phase by referring to the time of data acquisition. On the other hand, daily mean SST of OISST is assigned to wave phase at 00UTC of the day. We refer to these composites in Chapter 3 and 4.

Composites of values belonging to rainfall events are defined as summations over rainfall events, which are allocated into 32 wave phase bins, from $-\pi$ to π, and 2.5° latitude grid, divided by total numbers of pixels observed by TRMM PR, instead of total numbers of rainfall events. Since we employ orbit data, TRMM level 2 products, which only produce inhomogeneous sampling, this normalization is equivalent to unconditional mean. Another composite is zonal climatological mean, which is calculated in the same manner but using all rainfall events regardless of the wave phase bins with 2.5° latitude grid. Then we carry out independent two sample Student's *t*-tests on the wave phase composite and zonal climatological mean on each latitude. Here we consider rainfall events as independent each other. Anomalous values of composite mean are defined as differences between wave phase composite and zonal climatological mean. The composite of rainfall events is discussed mainly in Chapter 4 and used in Chapter 3.

The cloud fraction and radiative heating from CloudSat and CALIPSO products are also composited based on the wave phase with 32 bins and 2.5° latitude grid. Composite mean values are calculated as means of observational rays whose time and position correspond to the wave phase bin. The zonal-mean climatological composites are also made as means of all observations in 2.5° latitude grid. The independent two sample Student's *t*-tests are applied on the wave phase composite and zonal-mean climatology on each latitude. Anomalous values are defined as differences of wave phase composite from the climatology. Ascending and descending orbits are separately composited, and thus composites in daytime and nighttime are obtained respectively. We should note that the degree of freedom for two sample Student's *t*-test is defined as the number of observational rays of CloudSat/CALIPSO products divided by 40, which is the number of rays 1.4 km resolution in a 0.5° grid. These composite analyses are used in Chapter 5.

Figures and Tables

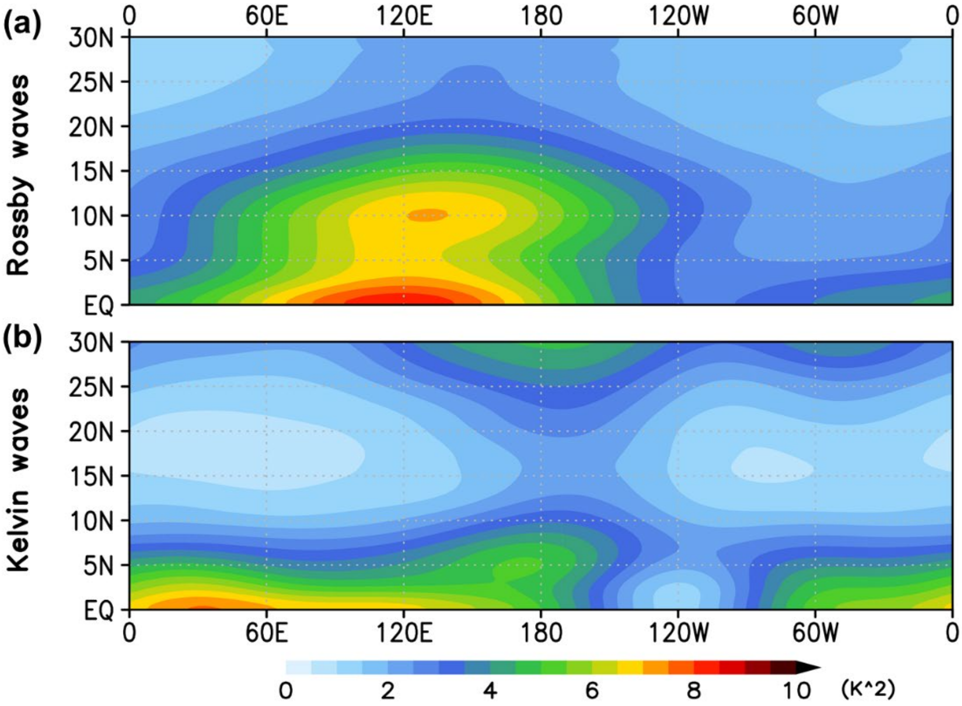

Fig. 2.1: Variances of filtered T_b with its filtering window shown in Table 2.1 for (a) Rossby waves, and for (b) Kelvin waves.

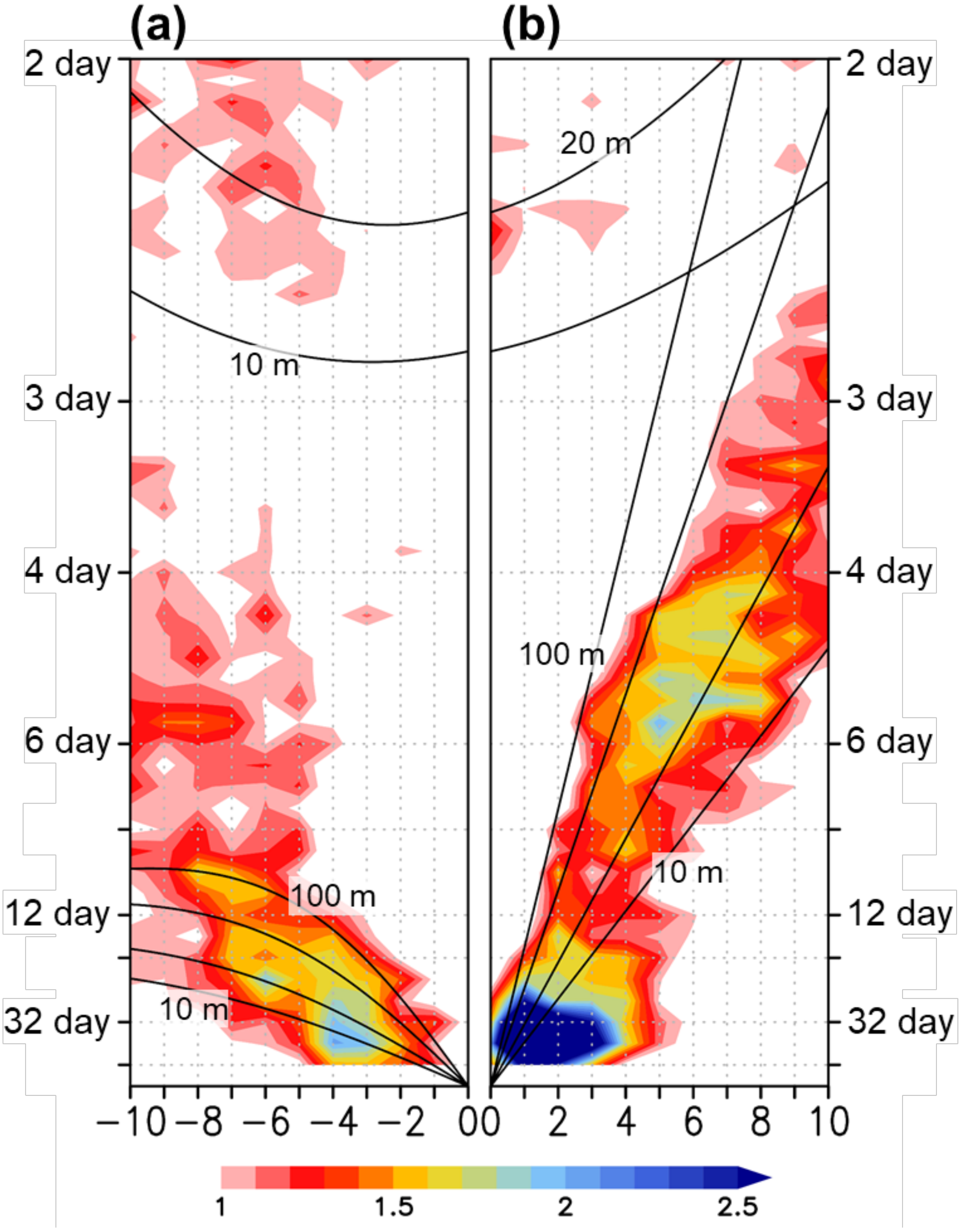

Fig. 2.2: Space-time spectra of symmetric T_b divide by its background red noise (a) for westward spectrum at 10°N and (b) for eastward spectrum at the equator. Black lines indicate dispersion curves of Kelvin wave and Rossby waves with 10, 20, 50, and 100 m of equivalent depths, and of inertia gravity wave with 10 and 20 m equivalent depths.

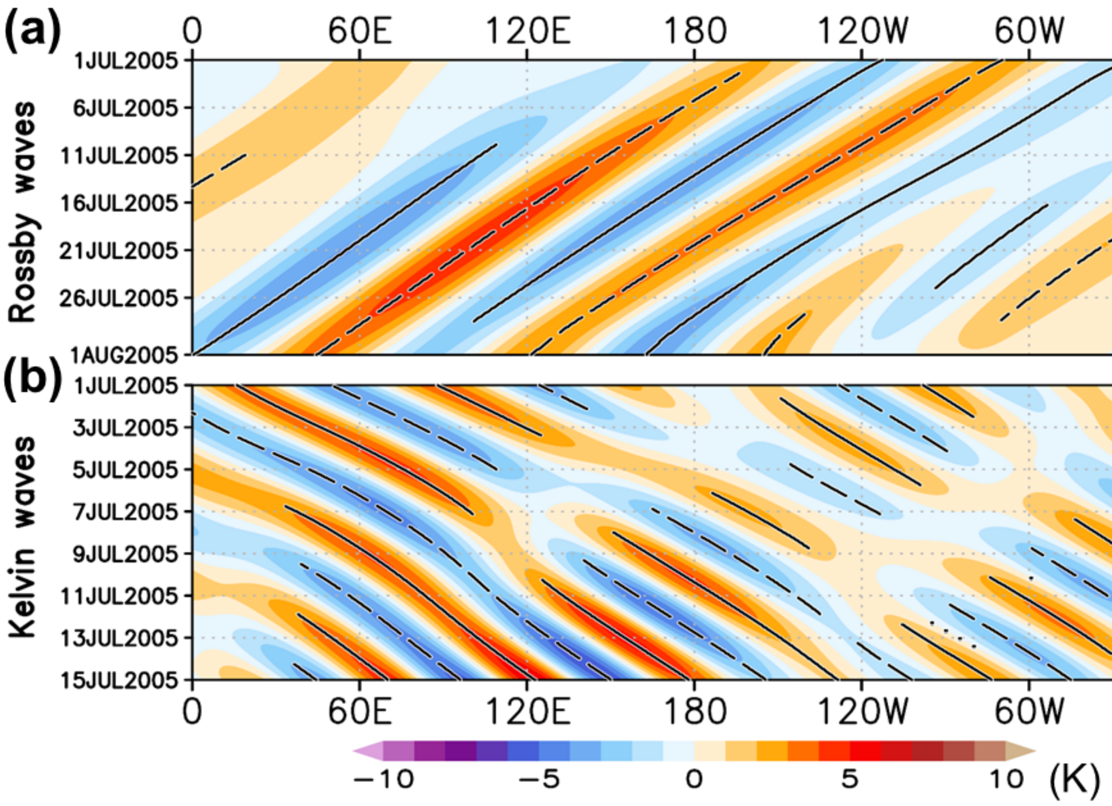

Fig. 2.3: The Hovmoller diagrams of filtered T_b (K) for (a) Rossby waves at 10°N and (b) Kelvin waves at the equator. Solid lines indicate wave phase $\pi/2$ and dashed lines indicate wave phase $-\pi/2$.

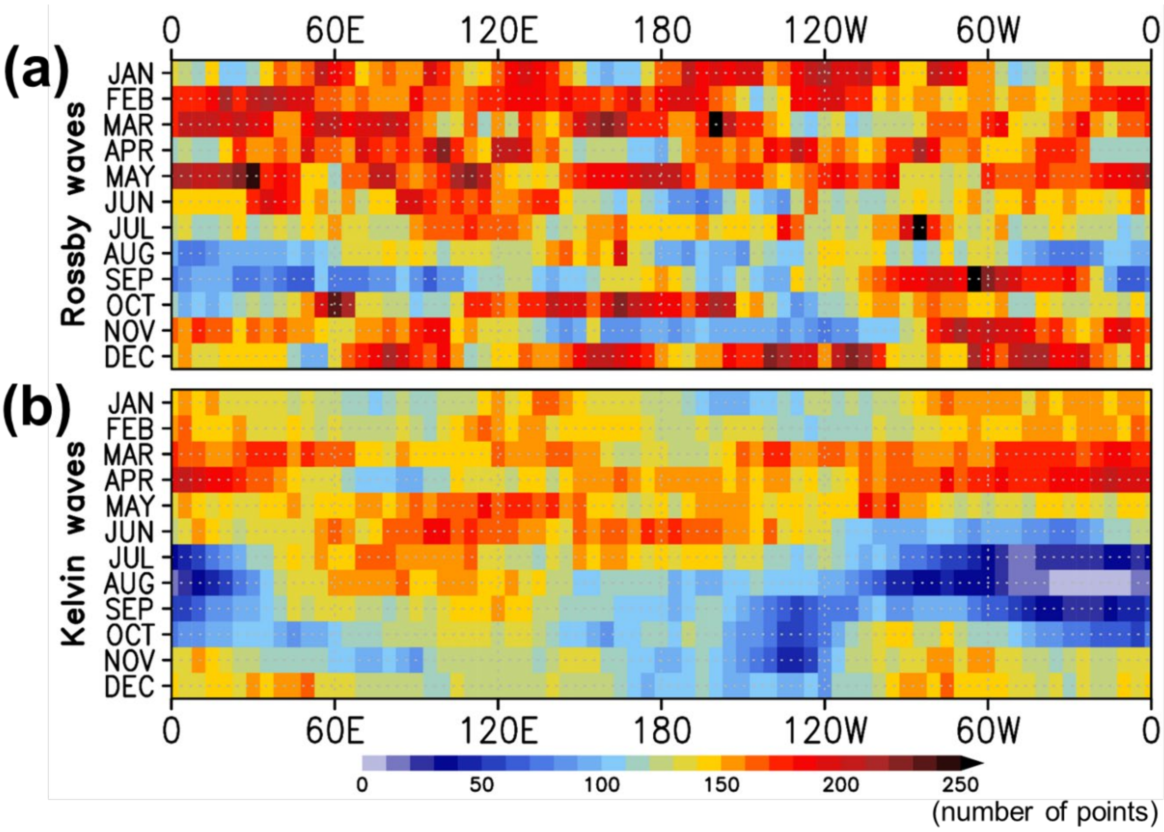

Fig. 2.4: Histograms of zonal and seasonal distribution of the number of minimum filtered T_b points that is referred as most convectively active point (a) for Rossby waves and (b) for Kelvin waves.

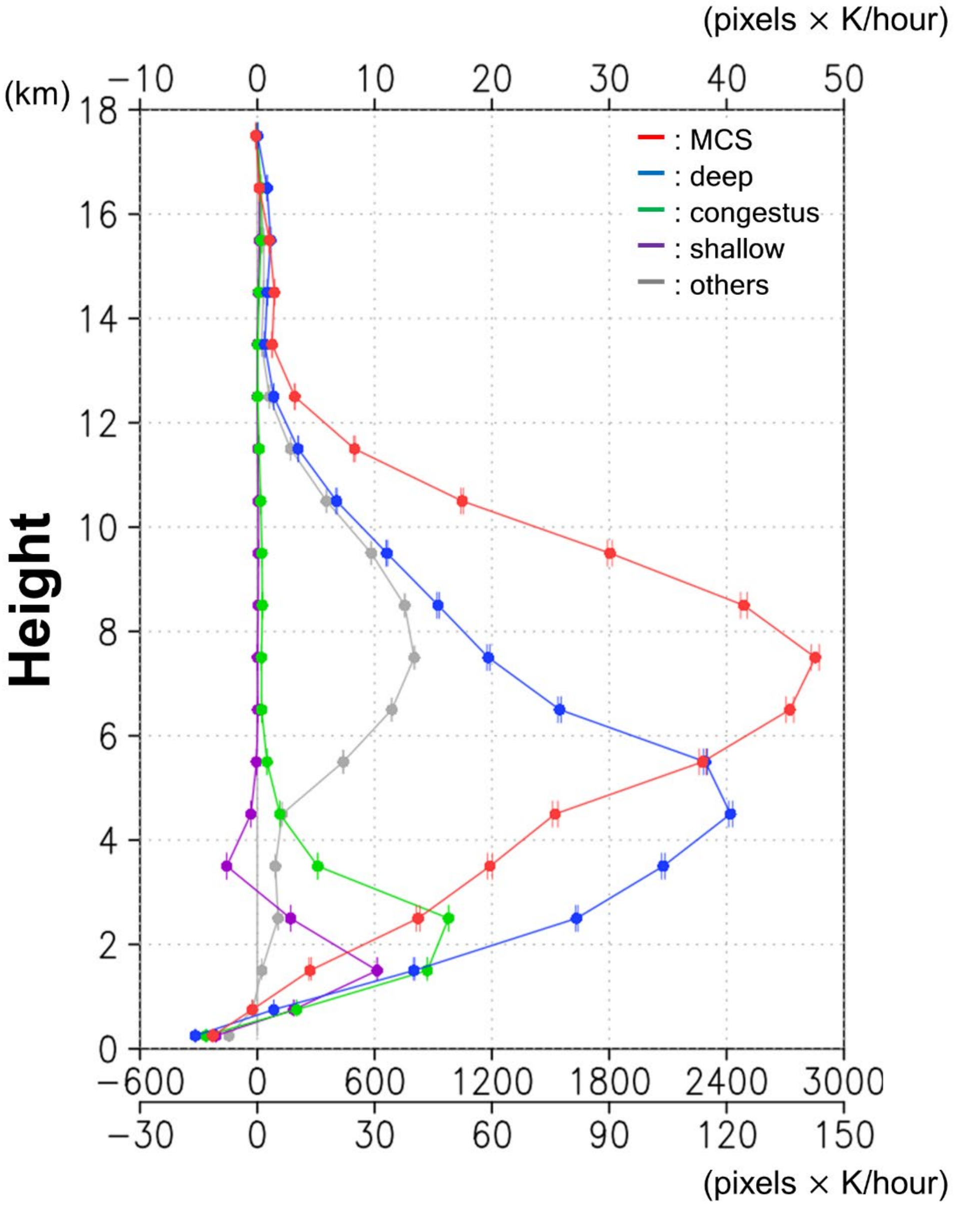

Fig. 2.5: Mean vertical profiles of volumetric convective heating $Q_1 - Q_R$ of rainfall events obtained from TRMM 2H25 product. The red, blue, green, purple, and gray lines show that of MCS, deep convection, congestus convection, shallow convection, and others, respectively. The mean values are calculated between 20°S-20°N, and analysis period. The error bars indicate the 99% confidence intervals. For the red and blue lines, refer to the upper and lower axes at the bottom, respectively. For the green, purple, and gray lines, refer to the axis at the top.

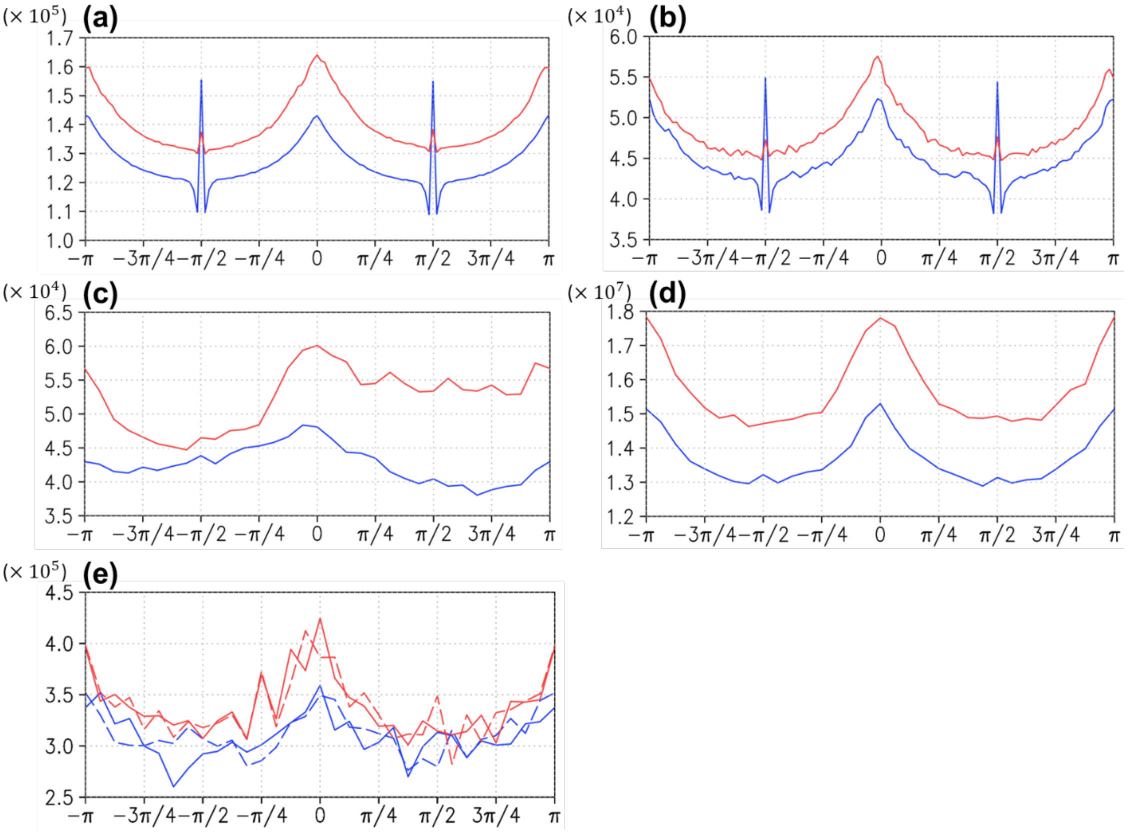

Fig. 2.6: The number of data points, which are allocated on the wave phase, of (a) ERA5 variables, (b) SSM/I variables, (c) rainfall events, (d) total pixels of TRMM PR, and (e) total pixels of CloudSat/CALIPSO products. For all panels, the red lines show Rossby waves on 10N and the blue lines show Kelvin waves on the equator. The solid lines in (e) indicate daytime orbit and the dashed lines in (e) indicate nighttime orbit.

Table 2.1: Summary of information of wave filtering.

	Wavenumber	Period (day)	Equivalent depth (m)	Reference latitude
Rossby	-5--2	12-48	10-100	10°N
Kelvin	4-8	4-6	10-100	EQ

Minimum T_b points	Autocorrelation time scale	Autocorrelation zonal spatial scale
31517	135 hour	25 degree
110315	30 hour	15 degree

Chapter 3.

Coupling mechanisms with analyses of wave structures and eddy energy budget

3.1. Introduction

Various coupling mechanisms between equatorial waves and convective activity have been suggested as reviewed in section 1.5. Adames et al. (2019) and Adames and Maloney (2021) summarized previous studies as contrasting groups: gravity wave mode group and moisture mode group. Furthermore, previous investigations on coupled convective activity reviewed in section 1.4 and on wave structures reviewed in section 1.2 strongly suggested that coupling mechanisms are different between Kelvin and Rossby waves.

Idealized numerical models suggested that these two unstable modes indicate different coupling regimes. Sobel and Bretherton (2003) showed two distinct forced waves in a non-rotating configuration. One was faster propagating that corresponds to the gravity wave, and the other was slower propagating or almost stational mode that is closely tied to moisture. Raymond and Fuchs (2007) constructed a convective parameterization which is sensitive to buoyancy and column moisture, and two unstable modes also appeared. One had vertically tilted structure that is forced by buoyancy-based precipitation, and the other had a vertically erect structure whose precipitation is mainly controlled by column moisture.

In this Chapter, we quantitatively discuss the suggested coupling mechanisms and their works on Rossby and Kelvin waves. The gravity wave mode is diagnosed based on the phase relationship between anomalous vertical motion and temperature, and the moisture mode is diagnosed based on the amplitude and maintenance of CWV fluctuation. Furthermore, we aim to make new quantitative description of eddy energy budget using the estimation of convective heating from TRMM product.

3.2. Data and Methodology

We conduct composite analyses of synoptic scale wave disturbances using the ERA5 reanalysis dataset (section 2.1.2, Hersbach et al. 2020), CWV fluctuations with SSM/I (section 2.1.5, Meissner and Wentz 2012; Wentz 2013), and SST anomalies using OISST (section 2.1.6, Reynolds et al. 2007; Huang et al. 2021). Detailed composite procedures are described in the previous section 2.2.3. For the composite field, the x-axis is the wave phase, and the y-axis and the z-axis are the latitude and pressure coordinates, respectively. In composite figures, one wavelength corresponds to wave phases from $-\pi$ to π. To investigate precipitation coupled with equatorial waves, we use the TRMM level 2 data products, 2A25 and 2H25 V7 (Iguchi et al. 2000; Shige et al. 2004, 2009; Takayabu and Tao 2020). We refer to sum of surface precipitation and total vertical apparent heat source and moisture sink ($Q_1 - Q_R$, Q_2, Yanai et al. 1973) of the rainfall event dataset, which is defined in section 2.1.3 and 2.1.4. Composites of values belonging to rainfall events are also described in the previous section 2.2.3.

3.3. Results

3.3.1. Structures of circulation and precipitation distributions

In the composite horizontal structures (Fig. 3.1), it is confirmed that the horizontal wind anomaly and T_b anomaly have equatorially symmetric structures for both waves. Because of the definition of the wave phase, the positive and negative maxima of T_b anomalies are either at $+\pi/2$ or at $-\pi/2$. The positive vorticity centers of Rossby waves lead and lag the negative T_b peak by about $\pi/4$ (Fig. 3.1a). Amplitudes of vortical circulations and T_b maximize almost in phase at 12-15 degrees and 10 degrees, respectively. Some weak but robust T_b anomalies also spread over the equator. In free wave solution (Matsuno 1966), Rossby waves indicate that horizontal convergence lag behind cyclonic circulation by 1/4 wavelength around off-equatorial region. Therefore, an importance of frictional convergence near the surface is suggested as discussed later. Kelvin waves (Fig. 3.1b), whose reference latitude is set to the equator, do not have meridional wind anomalies except near the center of horizontal convergence, which leads minimum T_b by about $3\pi/8$. Amplitudes of zonal winds and T_b are maximized on the equator. This symmetric pattern may be due to the global and annual composite and the choice of its reference latitude, whereas previous studies suggest that, for Kelvin waves, dynamical signals are more centered on the equator, while convection is located within the ITCZ over the Pacific Ocean (Straub and Kiladis 2002; Takayabu and Murakami 1991; Takayabu et al. 1999). To investigate the relationship between convective activity and circulation, we choose references on the latitudes that are most convectively active based on the following results in vertical cross sections. These latitudes are 10°N for Rossby waves and the equator for Kelvin waves.

We next produce composite figures for precipitation and CWV based on satellite observations (Fig. 3.2). Anomalous values from the climatological unconditional mean indicate almost symmetric distributions of precipitation and CWV. Precipitation distributions are close to horizontal convergence predicted by free wave characteristics and qualitatively consistent with the propagation characteristics shown in Lubis and Jacobi (2015). For Rossby waves, both positive and negative precipitation and CWV peaks clearly exist. The precipitation anomaly peak is at around $\pi/4$, and CWV anomaly peak is behind $\pi/2$. These two peaks lag about 1/8 wavelength. Their amplitudes in the Northern Hemisphere are larger than in the Southern Hemisphere. In contrast, Kelvin waves show weak but substantial positive CWV anomaly around $-\pi/2$, but do not have clear negative CWV anomalies, with anomalous values close to zero or even slightly positive around $\pi/2$, despite of the existence of negative precipitation anomalies. Weak but positive correlation between CWV and precipitation is confirmed especially in their positive anomalies. This feature is consistent with the absence of the spectrum peak of precipitable water (Roundy and Frank 2004). The positive precipitation anomaly maximum is found at $-\pi/4$, leading negative T_b anomaly with 1/8 wavelength.

The vertical cross sections show distinct differences between Rossby and Kelvin waves; a vertically upright structure for Rossby waves and a vertically tilted structure for Kelvin waves (Fig. 3.3). The structures have been investigated by statistical studies as Kiladis and Wheeler (1995) and Gonzalez and Jiang (2019) for Rossby waves and Straub and Kiladis (2002) for Kelvin waves. We obtained consistent results with statistical analyses using more recent dataset. As for Rossby waves, in the phase of active convection, low-level convergence and upper-level divergence are in phase and the upward motion is dominant, and their signs are reverse in the less precipitating phase (Fig. 3.3a). The low-level divergence signals have only weak statistical significance and are found below 800 hPa, which suggests that the frictional convergence of rotational flow in the boundary layer is an important factor, since the free wave solution show that horizontal divergence is in quadrature with vortical circulations, not in phase. Horizontal winds show that upper-level signals do not correspond to the free wave characteristics (Fig. 3.4a). The upper-level divergence can be considered as a response at the top of an ensemble of moist convection, such as deep cumulonimbi and cloud clusters. The low-level convergence signals are found in cyclonic circulations, and are inferred to be frictional (Fig. 3.4e).

For the Kelvin waves, the vertical tilted structure consists of a leading convergence near the surface at $\pi/4$ followed by a middle-level convergence and an upper-level divergence at $-3\pi/4$-$-\pi/2$ (Fig. 3.3b). In the convectively active phase, from $-\pi$ to 0, the horizontal convergence shifts upward and rearward in the lower troposphere, and vertical upwelling velocity grows deeper as wave phase progresses. This evolution of Kelvin wave circulation makes drastic transition of vertical structure of vertical motion. These characteristics are qualitatively consistent with those depicted in previous studies (Kiladis et al. 2009). It is confirmed that horizontal divergence signals are primary due to the zonal wind except for upper level (Fig. 3.4b, d, f). The off-equatorial wind anomalies remain significant in the upper and middle levels (Fig. 3.4b, d), which may reflect the interaction with the extratropics of Kelvin waves (e.g., Straub and Kiladis 2003b).

3.3.2. Vertical structures of thermodynamic and specific humidity

Vertical cross sections of the temperature anomalies are shown in Fig. 3.5. In the Rossby waves case, a large anomaly is notable at 300 hPa, and signals with an opposite sign exist in the lower half (Fig. 3.5a). These signals are centered at ±π/2, and thus are all in phase with convective activity. The structures in the lower free troposphere differ from previous studies. Kiladis et al. (2009) analyzed a positive temperature anomaly at 850 hPa and a negative anomaly at 700 hPa. In contrast, our results show two negative anomaly peaks at 800 hPa and 600 hPa centered at around $\pi/4$ and $\pi/2$, respectively. This inconsistency may be caused by differences in the composite method as well as the geographical distributions of the station of radiosonde observation by Kiladis et al. (2009).

Kelvin waves, on the other hand, have a vertically tilted structure (Fig. 3.5b). The temperature and omega anomalies indicate a nearly quadrature phase relationship at each level with some modifications with convection, thus Kelvin waves are strongly suggested to be assigned to the gravity wave mode. In lower layer from 900 to 500 hPa levels, ascending anomaly is modified to slightly lag behind expected gravity wave-like quadrature relationship of warm anomaly and in phase with near surface convergence at around $\pi/4$. In upper layer from 500 to 200 hPa levels, ascending anomaly is modified at around $\pi/2$ to be earlier than expected quadrature relationship. This modulation results in vertically deeper ascending that is tied to low-level horizontal convergence and that may be caused by convectively coupling.

The vertical cross sections of composite specific humidity are shown in Fig. 3.6. Rossby waves again show a vertically upright structure (Fig. 3.6a). The moisture anomaly peaks slightly lag behind phase ±π/2 and the precipitation anomaly (Fig. 3.2a). Compared to a previous study of Kiladis et al. 2009), the peak in the free troposphere is found at a lower level while the peak near the surface is weaker. This may be caused by the difference of dataset: in-situ observation and reanalysis. Since the synoptic condition with convergence at near surface, divergence in the upper troposphere, and a weak divergence around middle troposphere (Fig. 3.4a, c, e), associated with deep upwelling motion (Fig. 3.3a) can moisten free troposphere efficiently resulting CWV anomalies with large amplitude. When CWV shows a large positive anomaly, precipitation is encouraged (Bretherton et al. 2004; Peters and Neelin 2006). And on the other hand, when a large negative anomaly is provided, precipitation is strongly suppressed. Thus the dipole-like large CWV anomalies strongly suggests that convectively coupled Rossby waves include a moisture mode driven by CWV variability as a coupling mechanism as suggested in Gonzalez and Jiang (2019).

For Kelvin waves, on the other hand, vertical tilted specific humidity structure is found (Fig. 3.6b). The moist anomaly exists near the surface at the front side around $\pi/2$, where downward motion is dominant in the free troposphere, and convection is inactive. When the horizontal convergence becomes dominant (Fig. 3.3b) and the upwelling motion starts developing at $\pi/4$, the lower free troposphere becomes moist, but the middle level remains dry. Then the moist anomaly in the free troposphere spreads from the low troposphere to the middle troposphere as the wave phase progresses. In largely precipitating phase around $-\pi/2$ (Fig. 3.2b), the deep moist anomaly from the surface to upper troposphere with the deep ascending is indicated.

Meridional structure is more important for Rossby waves whereas Kelvin waves are confined to the equator and that seems intrinsic to its nature. Furthermore, three-dimensional construction was required to produce theoretical unstable mode that corresponds to Rossby waves (Fuchs-Stone et al. 2019). Thus, the meridional circulation of Rossby waves is investigated here.

To discuss Rossby waves' disturbances with the congestus convection, meridional cross sections of composite field are shown in Fig. 3.7. At $-\pi/2$, a large descent and dry anomaly strongly suppress convective activity, and stacked moist anomaly with a deep ascent activate MCS and deep convection at off-equatorial latitudes (Fig. 3.7a, c). Around the equator, downwelling anomaly can be seen around 400 hPa level but its statistical significance is low. A dry anomaly above 700 hPa level (Fig. 3.7a) and a warm anomaly on 600-500 hPa level (Fig. 3.7d), which may be caused by the descent, can prohibit deep development of convection, even though slight upward and moist anomaly below 800 hPa level can encourage congestus convection. We note here that the discrepancy of vertical structure of anomalous temperature in Rossby waves between Fig. 3.5a and the result shown by Kiladis et al. (2009) may be caused by the difference of meridional position in composite analyses (Fig. 3.7f).

3.3.3. Heating profiles and budget analysis of column moist static energy

Figure 3.8 shows the profile of convective heating, which is apparent heat source (Yanai et al. 1973) minus radiative heating, $Q_1 - Q_R$, produced in the TRMM 2H25 product. The sign of anomalous heating in the Rossby waves (Fig, 3.8a) switches at 0 and π, which is consistent with the sign of the precipitation anomaly. This is mainly composed by top-heavy heating, whose peak is located around 400 hPa level. The vertical profile of Kelvin wave heating anomaly transits from bottom-heavy into top-heavy (Fig. 3.8c) with larger amplitude than Rossby waves because of their larger positive precipitation anomalies (cf. Fig. 3.2). For both wave cases, the top-heavy heating is dominant in their maximum phase of precipitation and is in phase with upper-level anomalies of ascending and positive specific volume (Fig. 3.8b, d). Since top-heavy heating strongly indicates a dominance of organized convective systems (Houze 1989; Schumacher et al. 2004) and the upper-level heating anomalies are almost synchronized with temperature anomalies (cf. Fig. 3.5), latent heat release from organized convection can generate available potential energy (APE) to drive and maintain wave disturbances via kinetic energy supply.

Next, we examine the column-integrated budget of moist static energy (MSE) as follows,

$$\left\langle\frac{\partial\bar{h}}{\partial t}\right\rangle+\left\langle\bar{u}\frac{\partial\bar{h}}{\partial x}\right\rangle+\left\langle\bar{v}\frac{\partial\bar{h}}{\partial y}\right\rangle+\left\langle\bar{\omega}\frac{\partial\bar{h}}{\partial p}\right\rangle=H_{sfc}+\langle Q_R\rangle-\left\langle\frac{\partial}{\partial p}\overline{\omega'h'}\right\rangle=\langle Q_1\rangle-\langle Q_2\rangle \qquad (3.1)$$

Here, h is MSE, Q_1 and Q_2 are the apparent heat source and moisture sink, respectively (Yanai et al. 1973), Q_R is radiative heating, and H_{sfc} is the surface heat flux, which includes sensible and latent heat. The angle brackets denote column integration from 1000 hPa to 150 hPa. Above 150 hPa, wave structures might include stratospheric response (cf. Figs. 3.3, 3.5). The overbar denotes horizontal average and prime denotes deviation. Here, the scale of this horizontal average is the reanalysis grid, thus deviation means subgrid scale processes. The horizontal divergence of cross terms, $\left\langle\frac{\partial}{\partial x}\overline{u'h'}\right\rangle$ and $\left\langle\frac{\partial}{\partial y}\overline{v'h'}\right\rangle$, are assumed to be smaller than the vertical counterpart and are omitted. The composite analysis of each term in the lhs, the tendency and advection terms, are calculated in the same way as other variables: we make a time series and seasonal mean and then make anomalous composites. Additionally, surface heat flux and radiative heating are derived from the reanalysis dataset. The vertical convergence by vertical eddy transport is estimated from $\langle Q_1\rangle-\langle Q_R\rangle$ and $\langle Q_2\rangle$, which are estimated in the TRMM 2H25 product.

The MSE amplitude of Rossby waves is notably larger than that of Kelvin waves, while the precipitation amount amplitude is larger in the Kelvin waves case (Fig. 3.9a, b, and Fig.3.2). This larger amplitude of Rossby waves is largely due to moisture variance (cf. Fig. 3.5 and 3.6). That implies that Rossby waves are strongly controlled by MSE and/or moisture modulation. To investigate how MSE fluctuation is formed, each term in equation 3.1 is decomposed; total advection term is $-\left\langle\bar{u}\frac{\partial\bar{h}}{\partial x}\right\rangle-\left\langle\bar{v}\frac{\partial\bar{h}}{\partial y}\right\rangle-\left\langle\bar{\omega}\frac{\partial\bar{h}}{\partial p}\right\rangle$ (J/kg/sec) and forcing term is $H_{sfc}+\langle Q_R\rangle$ (J/kg/sec) in Fig. 3.9a and 3.9b, and each three advection terms, surface heat flux and radiative heating are in Fig. 3.9c and 3.9d.

In the Rossby waves case, the forcing term is almost in phase with MSE anomaly itself which indicates that forcing term mostly contributes to amplification and maintenance rather than propagation (Fig, 3.9a), and this is mainly controlled by radiative heating (Fig. 3.9c). The total advection term damps MSE fluctuation, and this damping advection mainly consists of vertical advection (Fig. 3.9c). In the convectively active phase, upwelling plays a role in advection (Fig. 3.3a). Zonal advection is almost in phase with the tendency and meridional advection shows only weak contribution. This may be caused by large zonal gradient of MSE or CWV.

In the Kelvin waves case, on the other hand, the total advection term makes significant contributions to MSE propagation, whereas forcing terms are against propagation (Fig. 3.9b). The vertical advection shows a large amplitude whereas the horizontal advection is nearly zero (Fig. 3.9d). Kelvin waves have almost no meridional wind and small CWV gradient, thus the horizontal MSE advection is small. The vertical advection corresponds with a tilted omega structure.

In both Rossby waves and Kelvin waves, the maximum peaks of CWV lag to that of MSE tendency with 1/4 wavelength (Fig.3.9e, f), and MSE itself corresponds with CWV (cf. Fig. 3.9a, b). This indicates that MSE fluctuations tightly connect to CWV in both types of waves. However, their amplitudes are starkly different in each wave. Rossby waves show large MSE fluctuation and small precipitation perturbation. In contrast, Kelvin waves show small MSE fluctuation and large precipitation perturbation (Fig. 3.2). This result strongly supports classifying Rossby waves as moisture mode and Kelvin waves as gravity wave mode. Precipitation coupled with Rossby waves is controlled by CWV and/or MSE, whereas precipitation coupled with Kelvin waves is controlled by buoyancy and/or dynamical disturbances.

Next, we quantify the amplitude of moisture mode and the generation of eddy APE and kinetic energy. According to the idealized description of moisture mode by Sobel and Maloney (2012), the growth of CWV is written as

$$\frac{\partial}{\partial t}\int \frac{1}{2}W^2 dx = -M_{eff}\int PW dx + \int \frac{H_{lh}}{L_c} W dx . \qquad (3.2)$$

Here, M_{eff} is effective gross moist stability, which is defined as $\widetilde{M}(1+r)-r$ in Sobel and

Maloney (2012) with normalized gross moist stability $\widetilde{M}$ and cloud-radiative feedback parameter r. The cloud-radiative feedback is omitted in this section, and r is set to 0. Detailed radiative processes are discussed later in Chapter 5. The normalized gross moist stability is calculated as a mean value at the reference latitude over wave phases from $-\pi$ to π of $\left(\left\langle\bar{u}\frac{\partial\bar{h}}{\partial x}\right\rangle+\left\langle\bar{v}\frac{\partial\bar{h}}{\partial y}\right\rangle+\left\langle\bar{\omega}\frac{\partial\bar{h}}{\partial p}\right\rangle\right)/\left\langle\bar{\omega}\frac{\partial\bar{s}}{\partial p}\right\rangle$ with the same composite procedure for ERA5 variables. Here the s is dry static energy. The value for M_{eff} is -0.1 for Rossby waves and -0.03 for Kelvin waves. W is CWV, P is precipitation, H_{lh} is surface latent heat flux, and L_c is latent heat of condensation. Horizontal integration is calculated from $-\pi$ to π with actual wavelength referring to Table 2.1, and the diffusion is neglected. This formulation implies the moisture mode is efficiently amplified when the anomalies of CWV and precipitation are closely in phase. Rossby waves indicate significantly large amplitude of CWV and high efficiency for its growth (Table 3.1). Rossby waves need 7.2 day at its growth rate to achieve mature amplitude, which is well short of Rossby waves' period. On the other hand, Kelvin waves show only slight CWV amplitude and weak amplification.

The growth as eddy disturbances are described as follows (cf. Nitta 1972):

$$\frac{\partial}{\partial t}\left\langle\frac{1}{2}\left(\overline{u'^2}+\overline{v'^2}\right)\right\rangle=-\frac{\partial}{\partial y}\langle\overline{\phi'v'}\rangle-\frac{\partial}{\partial p}\langle\overline{\phi'\omega'}\rangle-\langle\overline{\alpha'\omega'}\rangle, \tag{3.3}$$

$$\frac{\partial}{\partial t}\left\langle\frac{1}{2\sigma}\overline{\alpha'^2}\right\rangle=\langle\overline{\alpha'\omega'}\rangle+\frac{R_d}{pc_p\sigma}\langle\overline{\alpha'Q'}\rangle. \tag{3.4}$$

For these equations, overbar denotes average over one zonal wavelength, and prime denotes deviations. The angle brackets denote column integration same as Eq. 3.1. The α is specific volume and the ϕ is geopotential. The Q is latent heat, but Q_1-Q_R estimated in TRMM product is substituted here. The R_d is gas constant for dry air, the c_p is specific heat of dry air at constant pressure, and the σ is static stability parameter as constant. The terms of energy exchange between background and disturbances are small, thus they are omitted in Eqs. 3.3 and 3.4. The APE is generated by $\langle\overline{\alpha'Q'}\rangle$ and converted to kinetic energy by $\langle\overline{\alpha'\omega'}\rangle$ into kinetic energy. Since the anomalies of α', ω', and top-heavy heating are in phase especially upper levels (Fig. 3.8), Both waves have large growth of kinetic energy (Table 3.1). The Rossby waves need 4.5 day and the Kelvin waves need 2.2 day to reach mature amplitude.

The eddy MSE convergence plus surface heat flux is estimated in two ways: as a residual of budget terms in ERA5 and TRMM 2H25 product as follows,

$$H_{sfc} - \left\langle \frac{\partial}{\partial p} \overline{\omega' h'} \right\rangle = \left\langle \frac{\partial \bar{h}}{\partial t} \right\rangle + \left\langle \bar{u} \frac{\partial \bar{h}}{\partial x} \right\rangle + \left\langle \bar{v} \frac{\partial \bar{h}}{\partial y} \right\rangle + \left\langle \bar{\omega} \frac{\partial \bar{h}}{\partial p} \right\rangle - \langle Q_R \rangle = \langle Q_1 \rangle - \langle Q_2 \rangle - \langle Q_R \rangle. \quad (5)$$

Here $\left\langle \frac{\partial \bar{h}}{\partial t} \right\rangle + \left\langle \bar{u} \frac{\partial \bar{h}}{\partial x} \right\rangle + \left\langle \bar{v} \frac{\partial \bar{h}}{\partial y} \right\rangle + \left\langle \bar{\omega} \frac{\partial \bar{h}}{\partial p} \right\rangle - \langle Q_R \rangle$ is calculated in ERA5 and $\langle Q_1 \rangle - \langle Q_2 \rangle - \langle Q_R \rangle$ is from TRMM 2H25 product. Note that these two values are from different datasets. The calculation in ERA5 depend on synoptic scale motion, moisture, and radiation. On the other hand, the calculation in TRMM product include cloud microphysics (cf. Takayabu and Tao 2020). Despite the difference of dataset, it is confirmed that these two values are almost in phase qualitatively less than $\pi/4$ phase lag, although their amplitudes are five times different (Fig. 3.9g, h). There could be some factors for this large discrepancy, for example, differences in samplings. Above all, since convective activity is parametrized in the numerical model, there is no guarantee that eddy terms estimated with ERA5 represent quantitatively that of satellite observation estimates. This eddy term implies intensity of convective activity, therefore it is not surprised that it is in phase with precipitation anomaly. Another important implication is redistribution of MSE in vertical column. Though it is hard to make quantitative speculation here, this vertical eddy may resist about half of its damping via vertical advection.

To discuss the surface moisture flux, we conduct a composite analysis of surface wind speed using the SSM/I dataset. In the Rossby wave case (Fig. 3.10a), the anomalous composite of surface wind speed shows that high speed anomalies exist around the cyclonic flow, and low speed anomalies are found around anticyclonic flow. Latent heat release is concentrated in the convectively active region; thus, it may enforce only cyclonic circulations. Furthermore, the enhancement of surface latent heat flux around the cyclonic circulation with near surface convergence by cyclonic circulation (cf. Fig. 3.4f) can be a source of large amplitude of CWV. At the equator, there are no significant positive signals of easterly wind around phase $-\pi/2$ although trade winds climatologically prevail. This implies the role of surface evaporation on westward propagation of large CWV may limited. In the Kelvin waves case (Fig. 3.10b), the surface wind is stronger in the easterly wind and horizontal convergence phase. This suggests that enhanced surface moisture flux by the preceding easterly overlapping climatological trade wind produces the leading moist anomaly near the surface. Additionally, moisture supplied from the surface in the convective inactive phase can compensate for the dry anomaly in the free troposphere (cf. Fig. 3.6b) and may cause a near-zero CWV anomaly.

3.4. Summary and discussion

In this Chapter, we conduct composite analyses of wave disturbances based on the wave phase. Furthermore, we quantify precipitation amount and CWV based on satellite observations. The vertically upright structure of the Rossby waves induces the stacked column moisture. The frictional convergence by lower-level rotational flow (Fig. 3.3a, 3.4e) gathers the surface latent heat flux (Fig. 3.10a), and the deep ascending anomaly efficiently moisten the free troposphere (Fig. 3.6a), and they cause the column-integrated MSE with large amplitude. It is amplified by radiation, propagated by zonal advection, and damped by vertical advection. Precipitation anomaly is almost in phase with the CWV (Fig. 3.2a, Fig. 3.9e). This implies that convective activity can be activated with large CWV (Bretherton et al. 2004; Peters and Neelin 2006). The large amplitude of CWV and the high correlation between precipitation and CWV strongly suggest that the Rossby waves may amplify and/or maintain their CWV fluctuations through a feedback process with precipitation based on the formulation of Eq. 3.2 constructed by Sobel and Maloney (2012). Thus, the Rossby waves can be assigned into the moisture mode group for their convective coupling processes. Furthermore, since top-heavy diabatic heating is in phase with upper positive temperature or specific volume (Fig. 3.5a, 3.8a, b), it is inferred that organized convective systems play a role for the generation of eddy APE and kinetic energy. This, plus the fact that the disturbances retain their free wave's circulations well (Fig. 3.1, 3.4), suggests that the propagation of the convectively coupled Rossby waves may be rooted in Rossby waves' own westward propagation. On the other hand, the horizontal advection of MSE accounts for its tendency (Fig. 3.9c), and this implies that the Rossby waves may be driven by a moisture perturbation as in the MJO. The moisture mode for convectively coupled Rossby waves, which may hold wave's characteristics, can be different from that of the MJO, which is a relatively pure moisture perturbation.

The Kelvin waves have a vertically tilted structure, and its omega and temperature anomalies show nearly quadrature phase relationship (Fig. 3.5b), indicating the characteristics of the gravity wave. At $3\pi/4$, precipitation indicate a negative anomaly (Fig. 3.2b), but the near surface layer is moist (Fig. 3.6b). At $\pi/4$, the bottom-heavy heating starts to be positive (Fig. 3.8c), which implies either shallow cumulus or deep but isolated convection (Houze 1989), and the wave disturbances show a shallow ascending anomaly, a moist lower free troposphere, and dry middle troposphere. At $-\pi/4$, where precipitation reaches its maximum, top-heavy heating shows large positive anomaly, which implies a dominance of organized convection. The wave disturbance at this phase indicates low-level horizontal convergence, deeply moist, and upper warm anomaly. These evolutions indicate strongly suggest Kelvin waves have gravity wave mode with eddy kinetic energy supply by MCSs and of the moist anomalies from near the surface to middle free troposphere. This coevolution between heating profile from bottom-heavy to top-heavy and the moist anomaly from the surface to mid-troposphere may correspond to the moisture-stratiform instability proposed by Kuang (2008).

Although we use global and annual reference signals of convectively coupled Rossby and Kelvin waves, previous studies indicate that propagation characteristics can differ seasonally and regionally (e.g., Yang et al. 2007a,b,c). In this study, we intend to detect more essential coupling characteristics and compare the results with previous idealized models. The methodology in this study implicitly assumes full propagation as a wave, which enables us to compare and test some ideas in simple models to actual situations. However, growing and decaying processes are not captured in the composite figure along the wave phase space. Another benefit of this methodology is that using many composite points enables us to investigate more directly convective activity using TRMM level 2 data products.

The free equatorial waves are derived as linearly separable. However, the total values of CWV and apparent heat source may be more important for convective activity, although we investigate anomalous values statistically in this study. Future work will require further discussions of this problem over a wide range of scales including the convective subgrid scale, the equatorial wave scale, and seasonal or longer climatological scales.

An issue of determination and commonality of equivalent depths of Rossby and Kelvin waves still remains. Results shown in the present study and previous idealized models strongly suggest that coupling modes of these two waves are clearly different: Rossby waves correspond to moisture mode and Kelvin waves correspond to gravity wave mode. This difference cannot justify the commonality of equivalent depths. On the other hand, both waves are amplified by top-heavy heating via available potential energy generation (Fig. 3.8). Furthermore, both waves show vertically similar structure each other when heating is large: upper warm and lower cold, deeply moist, and top-heavy omega (cf. Fig. 3.5, 3.6). These similarities may support the commonality of equivalent depths, and we need further study and discussion.

Figures and Tables

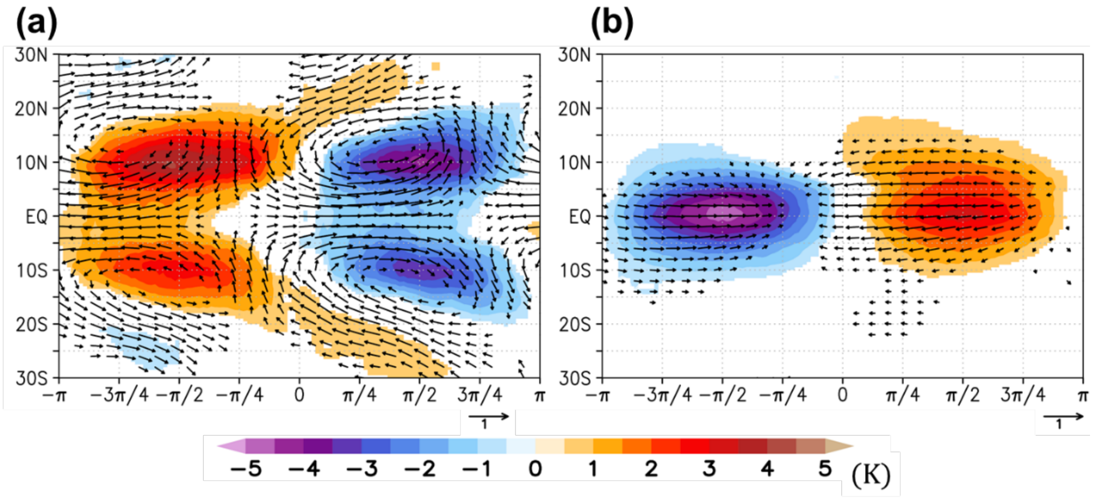

Fig. 3.1: Composite horizontal structures of brightness temperature anomalies (K; colors) and horizontal wind anomalies (m/s; vectors) at 850 hPa for (a) Rossby waves and (b) Kelvin waves. Shades for values over 95% confidence levels and vectors whose zonal or meridional component meet 95% confidence levels are plotted.

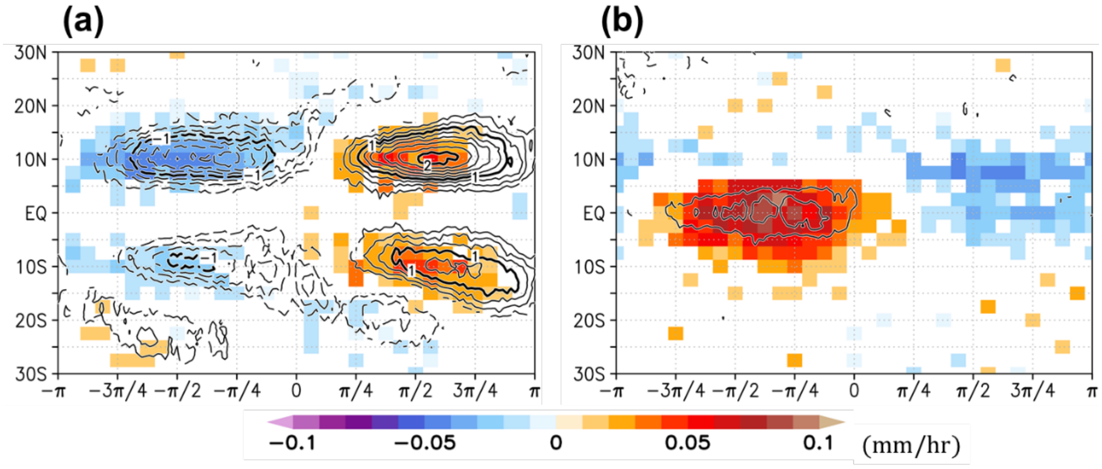

Fig. 3.2: Composite horizontal precipitation amount from rainfall events as unconditional mean (mm/hr; colors) and CWV derived from SSM/I (mm; contours with intervals of 0.2 mm) as anomalous values from climatology for (a) Rossby waves and (b) Kelvin waves. Grids and contours for values over 95% confidence levels are plotted.

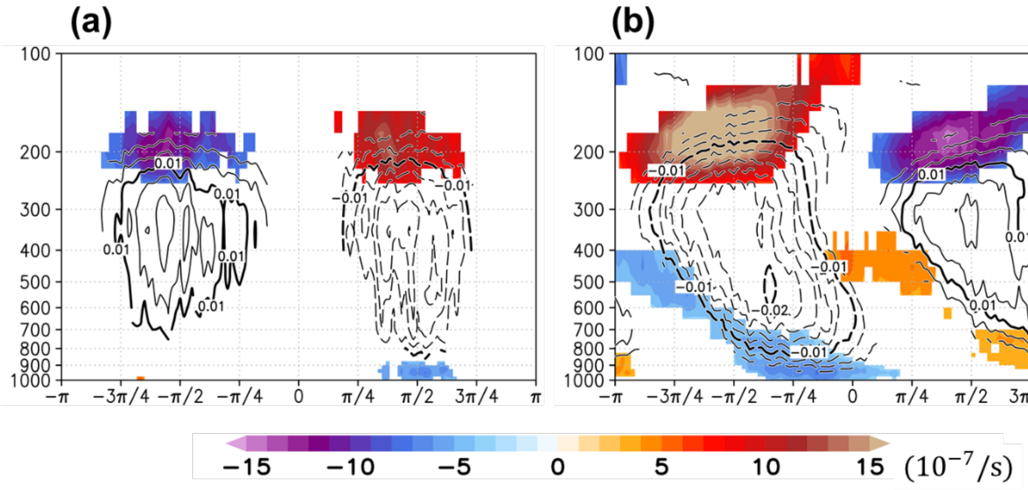

Fig. 3.3: Composite vertical structures of horizontal wind divergence (sec^{-1}; colors) and pressure velocity anomalies (Pa/s; contours with intervals of 0.002 Pa/s) for (a) Rossby waves at 10°N and (b) Kelvin waves at the Equator. Shades and contours for values over 95 % confidence levels are plotted.

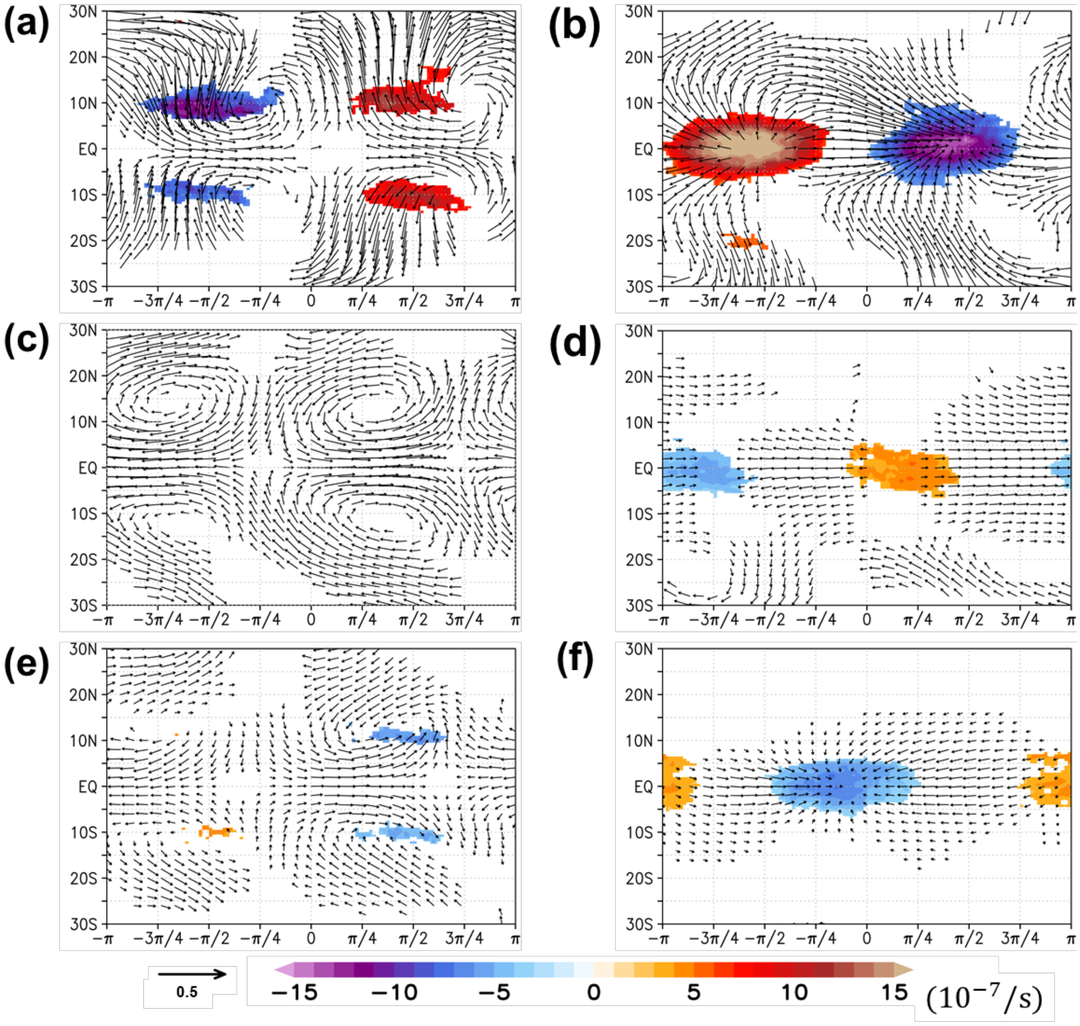

Fig. 3.4: Composite horizontal structures of horizontal wind (m/s; vectors) and its divergence (sec^{-1}; colors), at 200 hPa for (a) Rossby waves and (b) Kelvin waves, at 500 hPa for (c) Rossby waves and (d) Kelvin waves, and at 950 hPa for (e) Rossby waves and (f) Kelvin waves. Shades for values over 95% confidence levels and vectors whose zonal or meridional component meet 95% confidence levels are plotted. There are no significant shades in (c).

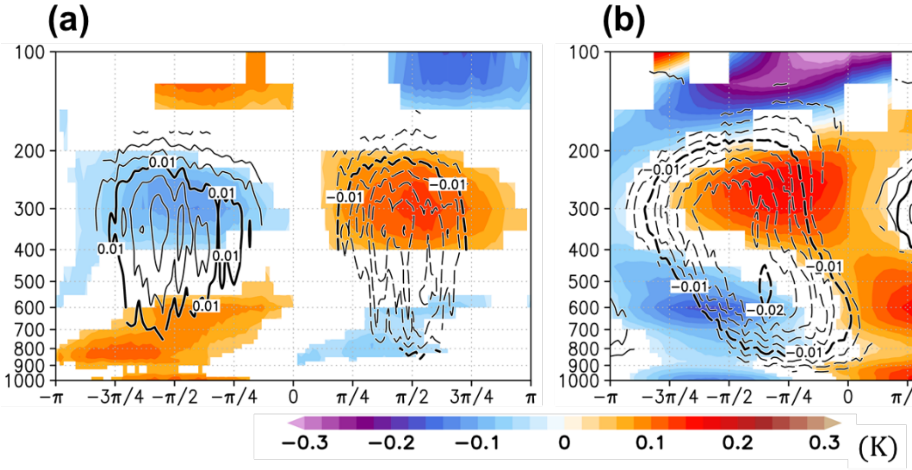

Fig. 3.5: Composite vertical structures of temperature anomalies (K; colors) and pressure velocity anomalies (Pa/s; contours with its interval of 0.002 Pa/s) for (a) Rossby waves at 10°N and (b) Kelvin waves at the Equator. Shades and contours for values over 95% confidence levels are plotted.

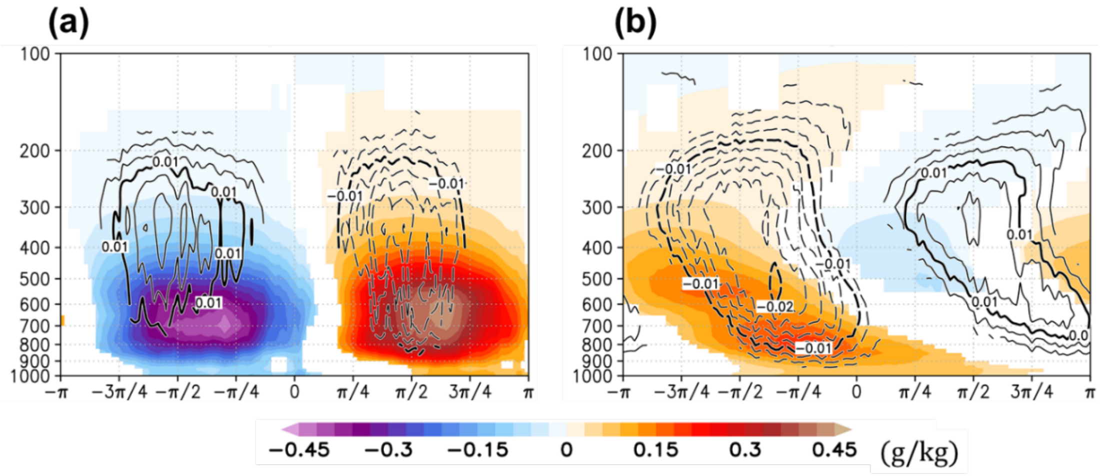

Fig. 3.6: Composite vertical structures of specific humidity anomalies (g/kg; colors) and pressure velocity anomalies (Pa/s; contours with intervals of 0.002 Pa/s) for (a) Rossby waves at 10°N and (b) Kelvin waves at the equator. Shades and contours for values over 95% confidence levels are plotted.

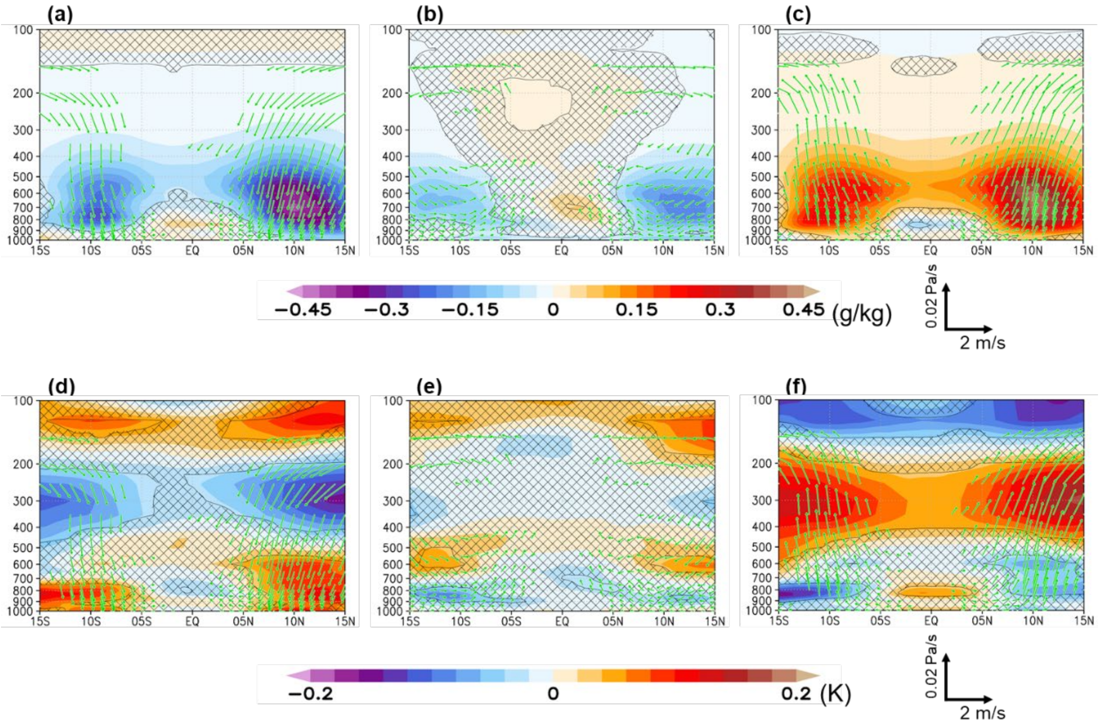

Fig. 3.7: Composites of meridional and vertical cross sections for Rossby waves of specific humidity anomalies (g/kg; colors) (a) at $-\pi/2$, (b) at 0, and (c) at $\pi/2$, and of temperature anomalies (K; colors) (d) at $-\pi/2$, (e) at 0, and (f) at $\pi/2$. Hatched area indicates that the anomalies which do not match 95% confidence levels. Green vectors are meridional-vertical motion and vectors whose meridional or vertical component meet 95% confidence levels are plotted.

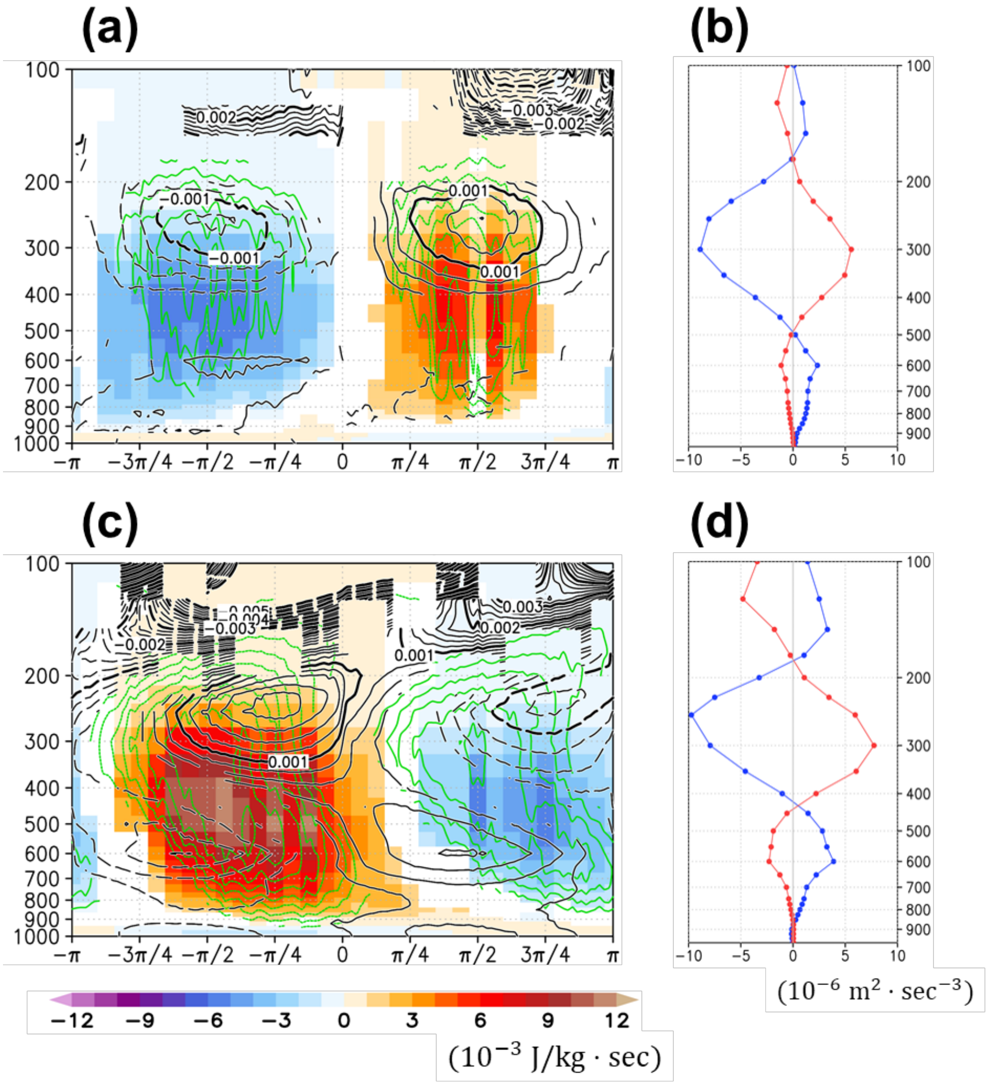

Fig. 3.8: Cross sections of composite of (a) estimated $Q_1 - Q_R$ anomaly (J/kg/sec; colors) derived from the TRMM 2H25 product whose vertical coordinate is converted into pressure from height, specific volume anomaly (m^3/kg; black contours with intervals of 2×10^{-4} m^3/kg), and pressure velocity (Pa/s; green contours with intervals of 0.002 Pa/s) for Rossby waves at 10°N and (b) vertical distribution of $\overline{\alpha'\omega'}$ (blue line) and $\frac{R_d}{pc_p}\overline{\alpha'Q'}$ (red line) for Rossby waves at 10°N. (c), (d) are same as (a) and (b) but for Kelvin waves at the equator.

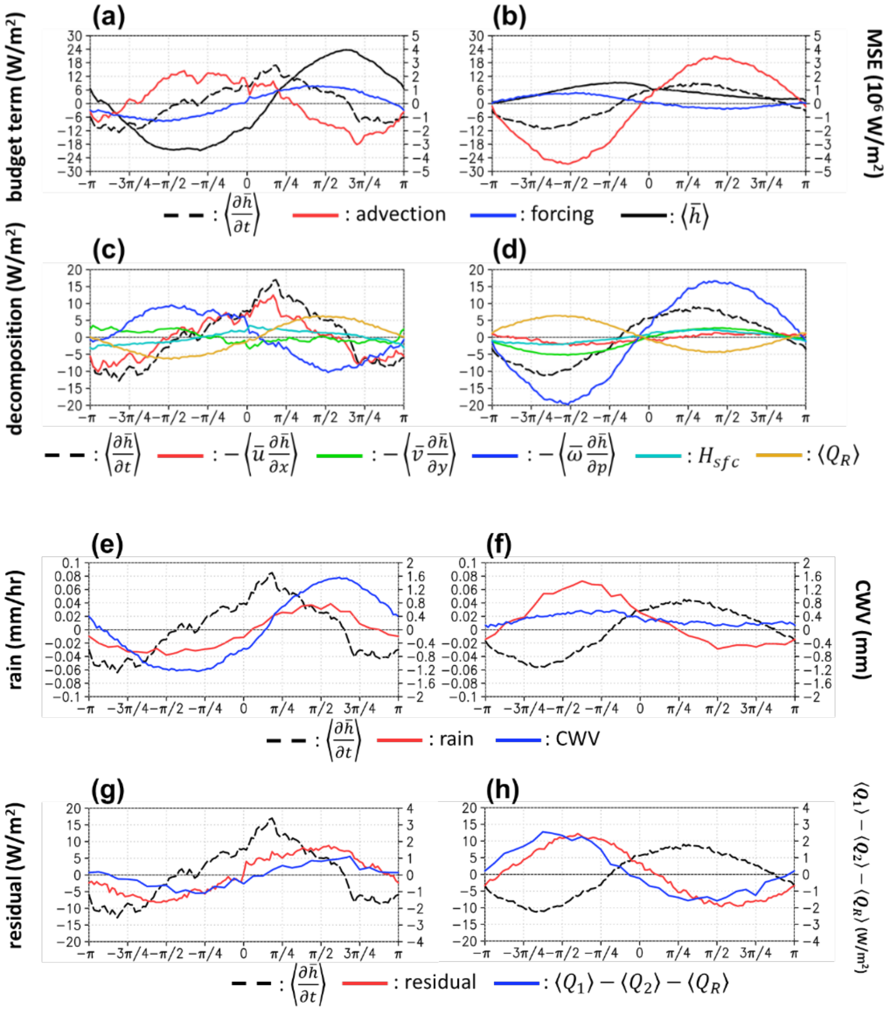

Fig. 3.9: Composite of column integrated MSE budget anomalies. The left column is for Rossby waves averaging from 5°N to 15°N and the right column is for Kelvin waves averaging from 5°S to 5°N. The bottom layer is 1000 hPa and top layer is 150 hPa for column integration. The y-axes for the black dashed line in (e, f) are omitted. Legends of lines are below each row. All terms are calculated with ERA5, except for rain in (e, f) and $\langle Q_1 \rangle - \langle Q_2 \rangle - \langle Q_R \rangle$ in (g, h) which are obtained from TRMM PR, and CWV in (e, f) which is obtained from SSM/I. Details of terms are described in the text.

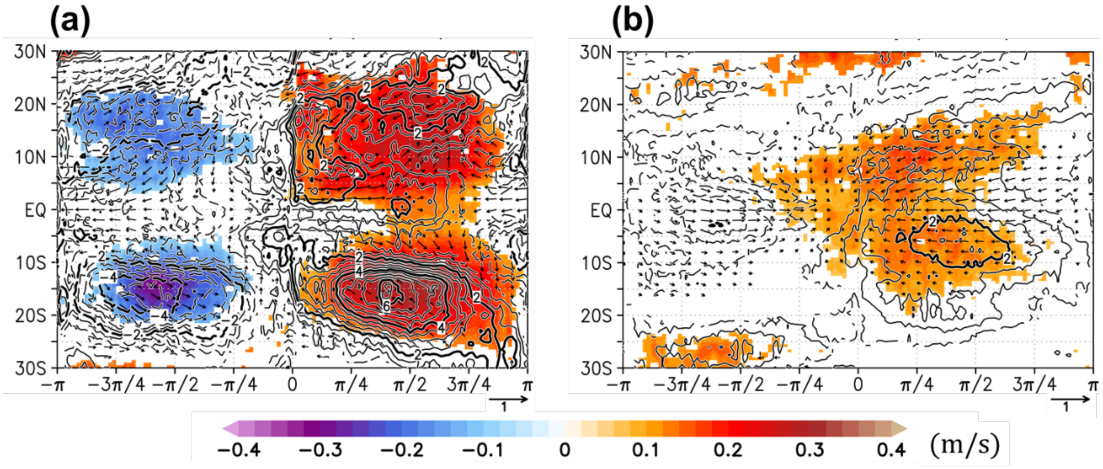

Fig. 3.10: Composite horizontal structures of horizontal wind speed anomalies derived from SSM/I (m/s; colors), surface latent heat flux estimated in ERA5 (J/m^2/s; contours with intervals of 0.5 J/m^2/sec), and horizontal wind (m/s; vectors) at 1000 hPa in ERA5 for (a) Rossby waves and (b) Kelvin waves. Shades and contours for values over 95% confidence levels and vectors whose zonal or meridional component meet 95% confidence levels are plotted.

Table 3.1: Estimated values of components for energy equations.

	$\int \frac{1}{2} W^2 dx$ (kg^2/m^3)	$-M_{eff} \int PW dx$ (kg^2/m^3/sec)	$\int EW dx$ (kg^2/m^3/sec)	$\left\langle \frac{1}{2} \left(\overline{u'^2 + v'^2} \right) \right\rangle$ (kg/sec^2)
Rossby	5.14×10^6	6.22	2.00	9.56×10^2
Kelvin	3.44×10^5	0.520	-0.103	5.84×10^2

$\left\langle -\frac{\partial}{\partial p} \overline{\phi' \omega'} \right\rangle$ (kg/sec^3)	$\left\langle -\frac{\partial}{\partial y} \overline{\phi' v'} \right\rangle$ (kg/sec^3)	$\langle -\overline{\alpha' \omega'} \rangle$ (kg/sec^3)	$\left\langle \frac{1}{2\sigma} \overline{\alpha'^2} \right\rangle$ (kg/sec^2)	$\left\langle \frac{R_d}{p c_p \sigma} \overline{\alpha' Q'} \right\rangle$ (kg/sec^3)
-1.67×10^{-3}	-3.46×10^{-3}	7.60×10^{-3}	3.29×10^2	4.91×10^{-3}
-3.75×10^{-3}	3.09×10^{-3}	3.68×10^{-3}	6.66×10^2	4.57×10^{-3}

Chapter 4.

Detailed precipitation characteristics

本章については、5年以内に雑誌等で刊行予定のため、非公開。

Chapter 5.

Cloud distributions and its radiative effects

本章については、5年以内に雑誌等で刊行予定のため、非公開。

Chapter 6.
General Conclusion

6.1. Summary

We utilize multiple satellite observational data products and quantitatively depict convective activities and cloud-radiative profiles with comparisons to previously suggested coupling mechanisms. First, the TRMM PR observation is used. The TRMM observation produces 3-dimensional distribution of precipitation, which directly capture detailed characteristics of rainfall event. Convective heating profile dataset retrieved based on the 3-dimensional precipitation data is also utilized. Second, we utilize CloudSat and CALIPSO satellite data, which provide properties of the cloud fraction and the radiative heating profiles. The accumulation of observational data and long-term statistical analyses enable us to further estimate the total diabatic heating for the first time by combining convective heating obtained from TRMM with radiative heating obtained from CloudSat/CALIPSO. This is an important advantage of this study.

In Chapter 3, theoretically derived hypotheses, such as the gravity wave mode and the moisture mode, are quantitatively examined with composite analyses for the Rossby and the Kelvin waves. We show that the Kelvin waves correspond to the gravity wave mode with a nearly quadrature phase relationship between the anomalies of vertical motion and temperature, and the Rossby waves correspond to the moisture mode in terms of the large CWV anomalies and its amplification. The convective heating $Q_1 - Q_R$ is also quantified, and we discussed its effect on the eddy energy budget based on the TRMM observation for the first time. The top-heavy heating from the MCSs dominates the eddy available potential energy (EAPE) generation in both waves. The detailed vertical distributions of the EAPE generation terms are shown utilizing satellite dataset, and they are similar in both waves with their peaks around 300 hPa level.

The detailed evolutions of precipitation characteristics are newly revealed in Chapter 4, by the 5-type classification of TRMM rainfall events. The MCSs and the deep convective events are simultaneously activated in the Rossby wave composite, while the shallow and congestus convective events occur in the later period of the convectively suppressed phase. On the other hand, in the Kelvin wave composite, a 5-type evolution from the shallow convective events to the decaying MCSs is shown. Despite these differences of evolutions, the MCSs contribute the most to precipitation amount in both waves. This similarity corresponds to the top-heavy heating profiles shown in Chapter 3.

Finally in Chapter 5, the cloud properties and radiative heating Q_R are quantified using CloudSat and CALIPSO data product. The composite results of CloudSat/CALIPSO are consistent to the former result of precipitation characteristics, obtained from TRMM rainfall events. Thus, the further estimation of the total diabatic heating Q_1, by combining radiative heating with convective heating, is achieved for the first time. This quantification reveals that the EAPE generation is increased by radiation by 30% in Rossby waves and by 42% in Kelvin waves. While the shortwave can amplify the EAPE generation in both waves, the longwave radiation indicates a contrasting role on the EAPE generation: reduction in the Rossby waves and increasing in the Kelvin waves. Additionally, the radiative heating shift the peak of EAPE generation to slightly upper level especially in the Kelvin wave composite.

6.2. Characteristics of convective coupling of Rossby waves

Findings of this study for the Rossby waves are schematically summarized in Fig. 6.1a, c. The Rossby waves have the vertically erect structure (Fig. 3.3, 3.5, 3.6). The moist and ascending anomalies are dominant over almost all troposphere. This erect and deeply moist synoptic condition can induce the CWV anomalies with large amplitudes. Since the anomalies of CWV with large amplitude at are almost in phase with precipitation anomaly (Fig. 3.9e), the moisture mode is strongly suggested as a coupling mechanism of the Rossby waves based on the construction of Eq. 3.2. The frictional convergence near the surface (Fig. 3.3a, 3.4e, 3.9c) can maintain large column moisture. In the phase of large CWV, the deep convective events, the MCSs, and the stratiform anvil rain are simultaneously activated (Fig. 4.7a), and the MCSs mainly contribute to precipitation amount. The large CWV may encourage deep development of convective towers and their organization with stratiform rain. This dominance of the MCSs with top-heavy heating is synchronized with the upper warm anomaly and can support the Rossby waves' growth and/or maintenance through EAPE generation (Fig. 3.8a, Table 3.1). Additionally, radiative heating plays a role on the amplification of the EAPE generation by 30% (Fig. 5.3, 5.4, Table 5.2). Shortwave strongly shows positive effect but longwave reduces the EAPE generation. The shallow and congestus convective events are active in the later part of the convectively suppressed phase due to high SST (Fig. 4.7c, 4.8a), which may be resulted from the clear sky with less precipitation.

6.3. Characteristics of convective coupling of Kelvin waves

Findings of this study for the Kelvin waves are schematically summarized in Fig. 6.1b, d. The Kelvin waves have the vertically tilted structure (Fig. 3.3, 3.5, 3.6). The anomalies of temperature and vertical motion show the phase shift with almost $1/4$ wavelength (Fig. 3.5b). This is highly consistent to gravity wave, and thus the gravity wave mode is strongly suggested as a coupling mechanism of the Kelvin waves. Since this phase shift is modulated in the upper layer, the peaks of these anomalies are close around 300 hPa level (Fig. 3.5b). The moist anomaly grows from near the surface layer to middle troposphere (Fig. 3.6b). However, the CWV anomaly does almost not show negative value and only small amplitude (Fig. 3.9f, Table 3.1). This implies that the moisture mode is dismissed for the Kelvin waves. The clear 5-type evolution of precipitation characteristics is indicated

(Fig. 4.7b, d): the shallow, congestus, deep convective events, the MCSs, and the stratiform anvil rain. This is consistent to the self-similarity suggested by Mapes et al. (2006). Here, their phase relationships and amplitudes are newly quantified. The MCSs mainly contribute to precipitation amount and the EAPE generation. The top-heavy heating of the MCSs is in phase with positive peaks of temperature and vertical motion anomalies (Fig. 3.8c, Table 3.1). On the other hand, the distinct deep but not organized convection induces bottom-heavy heating (Fig. 4.7b, 3.8c). Furthermore, radiative heating plays a role on the amplification of the EAPE generation by 42% (Fig. 5.4, Table 5.2). Both shortwave and longwave radiation indicate amplification effect (Fig. 5.2).

6.4. Discussions and future works

The Rossby waves indicate the features of the moisture mode in terms of the large anomalous CWV fluctuation, which is amplified or maintained through precipitation anomaly in phase (Eq. 3.2, Table 3.1, Fig. 3.9e). However, that is different from speculations by previous studies. In the framework constructed by Sobel and Maloney (2012), propagation characteristics of moisture mode disturbances were mainly controlled by surface moisture fluxes. Fuchs-Stone et al. (2019) speculated that preceding shallow convection on the equator plays a role on moisture supply via its pre-conditioning effect. However, the results of this study are not consistent as follows. First, the positive peak of CWV lags behind that of precipitation amount (Fig. 3.9e), and the moisture supply due to frictional convergence at the surface may amplify rather than propagate Rossby waves' CWV fluctuations (Fig. 3.4e, 3.9e, and Table 3.1). Second, the preceding shallow and congestus convection seem to be embedded in Rossby waves' circulation (Fig. 3.7, 4.7, 4.9) rather than play a pre-conditioning role. These suggest that the moisture mode works as connection and amplification between convective activity and large CWV, and propagation characteristics is controlled by that of Rossby wave itself. On the other hand, we should note that the tendency of column integrated MSE attributed to its horizontal advection (Fig. 3.9c). This implies that the moisture perturbation drives westward propagation of Rossby waves. A comparative study between MJO and convectively coupled Rossby waves is required to improve our understanding on the moisture mode.

The evolutions of precipitation characteristics shown in Chapter 4 and the transitions of cloud and radiative properties shown in Chapter 5 quantify the phase relationships between the first and the second baroclinic modes. The Rossby waves indicate that the first and the second baroclinic modes are almost in phase (Fig. 3.8, 4.7, 5.3). On the other hand, the Kelvin waves indicate the phase shift of about 1/8 wavelength between the two modes. This phase shift was often assumed empirically in idealized model studies (e.g. Khouider and Majda 2008), thus the quantitative findings of the phase relationships may contribute to constructions of theoretical framework.

In Chapter 4, we create histograms of the three indices. However, since we cannot determine the shape and relative position to background wind of each rainfall event in present dataset, these histograms have not sufficiently depicted behaviors of individual rainfall event. For example, we cannot analyze whether the organized systems are like squall lines or cloud clusters, and if they are an up-shear-tilted or down-shear-tilted eddy, although this information is important for turbulent scale processes such a convective momentum transport (Moncrieff 1992), whose importance in MJO has been suggested by Miyakawa et al. (2012). We need a further study on detailed rainfall event characteristics to clarify the smaller scale processes of momentum and/or moisture budget between convection and equatorial waves.

The contrast nature between gravity wave mode and moisture mode is emphasized in previous studies. However, we show common features as mean vertical profiles of EAPE generation (Fig. 3.8, 5.4). In both waves, the generation term is maximized around 300 hPa level and slightly negative around 600 hPa level. Furthermore, radiative heating strength its amplitude. The radiative heating in the Kelvin wave composite shifts the peak of the generation term upward (Fig. 5.4b). This may correspond to the spectrum peak of the Kelvin waves, which locates around dispersion curve of deeper equivalent depth than that of Rossby waves (Fig. 2.2). This might claim that the determination of equivalent depths depends on vertical structure of the EAPE generation, and common equivalent depths may be resulted from the dominance of top-heavy heating of MCSs. While this similarity of the vertical profile of EAPE generation is mean state over one wavelength, the detailed precipitation characteristics differs in terms of the phase relationship between deep convection and MCS, or the first and the second baroclinic modes. Further investigation is required to quantify equivalent depths and estimate how this phase relationship modulate equivalent depths.

Analyses in this study is expected to be applied to other equatorial wave modes and the MJO in various spatiotemporal-scale filtering. Previous studies implied that the choice of values of wavenumber or frequency for wave filtering may modulate results, especially in the case of Kelvin waves. Yasunaga and Mapes (2014) suggested that differences on modulations to convective activity from faster or slower propagating convectively coupled waves, and Roundy (2012) indicated the gradual transition from Kelvin wave to the MJO as the filtering band is changed to shallower equivalent depths. A contrast between the gravity wave mode and the moisture mode may depend not only on equatorial wave modes but on wave's spatiotemporal scale. An extension of composite analyses to wider spatiotemporal scales will reveal details of various coupling disturbances, and that can improve a theoretical approach based on the diabatic heating which is required as a future work to shed light on determination processes of equivalent depths of CCEWs.

Figures

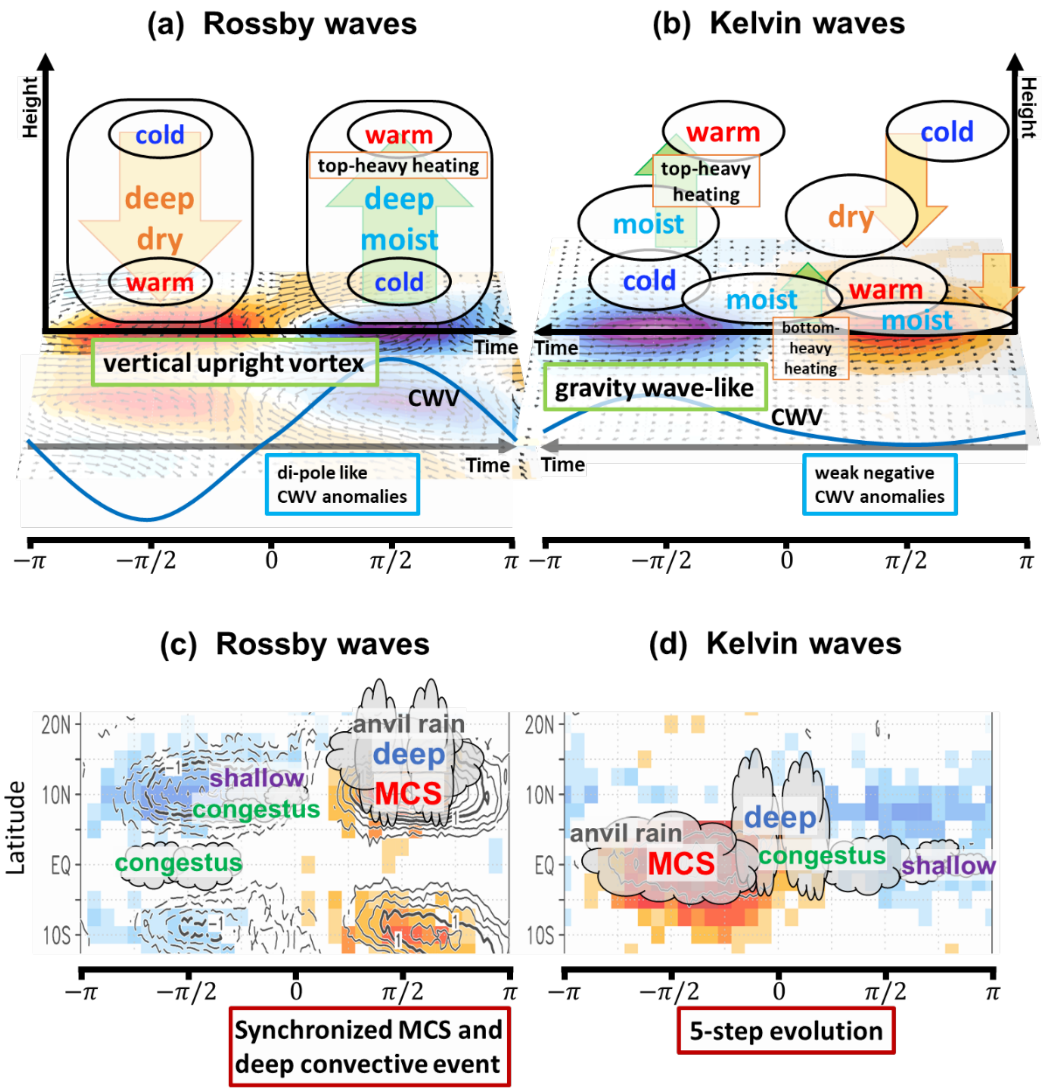

Fig. 6.1: Schematic figures of wave disturbances in upper panels and coupled precipitation characteristics in lower panels. The upper panels show the synoptic wave disturbances which is discussed in Chapter 3: humidity, temperature, vertical motion, and heating profile for (a) Rossby waves and for (b) Kelvin waves. The lower panels show distributions of precipitation characteristics with the anomalies of precipitation amount (color) and CWV (contour) which is discussed in Chapter 4, for (c) Rossby waves and for (d) Kelvin waves.

Acknowledgement

I sincerely acknowledge Prof. Y. N. Takayabu. She has continued supporting me to complete this study. I thank to Dr. K. Kikuchi who kindly provided to me the T_b dataset. I also acknowledge Profs. H. Miura, M. Satoh, T. Tozuka, and T. Miyakawa. They kindly reviewed this dissertation and gave me suggestive and constructive comments. I acknowledge to Prof. K. Suzuki and Dr. M. Chikira who often gave me helpful comments and discussions in seminars. I also thank to members of our laboratory for their support.

References

Adames, Á. F., and D. Kim, 2016: The MJO as a Dispersive, Convectively Coupled Moisture Wave: Theory and Observations. *J. Atmos. Sci.*, **73**, 913–941, https://doi.org/10.1175/JAS-D-15-0170.1.

——, and E. D. Maloney, 2021: Moisture Mode Theory's Contribution to Advances in our Understanding of the Madden-Julian Oscillation and Other Tropical Disturbances. *Current Climate Change Reports*, **7**, 72–85, https://doi.org/10.1007/s40641-021-00172-4.

——, D. Kim, S. K. Clark, Y. Ming, and K. Inoue, 2019: Scale Analysis of Moist Thermodynamics in a Simple Model and the Relationship between Moisture Modes and Gravity Waves. *J. Atmos. Sci.*, **76**, 3863–3881, https://doi.org/10.1175/JAS-D-19-0121.1.

Ahmed, F., and C. Schumacher, 2015: Convective and stratiform components of the precipitation ‐ moisture relationship. *Geophys. Res. Lett.*, **42**, https://doi.org/10.1002/2015gl066957.

Arakawa, A., and W. H. Schubert, 1974: Interaction of a Cumulus Cloud Ensemble with the Large-Scale Environment, Part I. *J. Atmos. Sci.*, **31**, 674–701, https://doi.org/10.1175/1520-0469(1974)031<0674:IOACCE>2.0.CO;2.

Awaka, J., T. Iguchi, H. Kumagai, and K. Okamoto, 1997: Rain type classification algorithm for TRMM precipitation radar. *IGARSS'97. 1997 IEEE International Geoscience and Remote Sensing Symposium Proceedings. Remote Sensing - A Scientific Vision for Sustainable Development*, Vol. 4 of, 1633–1635 vol.4.

Awaka, J., T. Iguchi, and K. Okamoto, 2007: Rain Type Classification Algorithm. *Measuring Precipitation From Space*, 213–224, https://doi.org/10.1007/978-1-4020-5835-6_17.

——, ——, and ——, 2009: TRMM PR Standard Algorithm 2A23 and its Performance on Bright Band Detection. *Journal of the Meteorological Society of Japan*, **87A**, 31–52, https://doi.org/10.2151/jmsj.87A.31.

Betts, A. K., and M. J. Miller, 1986: A new convective adjustment scheme. Part II: Single column tests using GATE wave, BOMEX, ATEX and arctic air ‐ mass data sets. *Quarterly Journal of the Royal*,.

Bretherton, C. S., M. E. Peters, and L. E. Back, 2004: Relationships between water vapor path and precipitation over the tropical oceans. *J. Clim.*, **17**, 1517–1528, https://doi.org/10.1175/1520-0442(2004)017<1517:rbwvpa>2.0.co;2.

Brown, R. G., and C. Zhang, 1997: Variability of midtropospheric moisture and its effect on cloud-top height distribution during TOGA COARE. *J. Atmos. Sci.*, **54**, 2760–2774, https://doi.org/10.1175/1520-0469(1997)054<2760:vommai>2.0.co;2.

Bryan, G. H., and M. J. Fritsch, 2000: Moist Absolute Instability: The Sixth Static Stability State. *Bull. Am. Meteorol. Soc.*, **81**, 1207–1230, https://doi.org/10.1175/1520-0477(2000)081<1287:MAITSS>2.3.CO;2.

Del Genio, A. D., Y. Chen, D. Kim, and M.-S. Yao, 2012: The MJO transition from shallow to deep convection in CloudSat/CALIPSO data and GISS GCM simulations. *J. Clim.*, **25**, 3755–3770, https://doi.org/10.1175/jcli-d-11-00384.1.

Dias, J., N. Sakaeda, G. N. Kiladis, and K. Kikuchi, 2017: Influences of the MJO on the space ‐ time organization of tropical convection. *J. Geophys. Res.*, **122**, 8012–8032, https://doi.org/10.1002/2017jd026526.

Fuchs, Ž., and D. J. Raymond, 2002: Large-Scale Modes of a Nonrotating Atmosphere with Water Vapor and Cloud–Radiation Feedbacks. *J. Atmos. Sci.*, **59**, 1669–1679, https://doi.org/10.1175/1520-0469(2002)059<1669:LSMOAN>2.0.CO;2.

Fuchs, Z., and D. J. Raymond, 2005: Large-scale modes in a rotating atmosphere with radiative–convective instability and WISHE. *J. Atmos. Sci.*, **62**, 4084–4094, https://doi.org/10.1175/jas3582.1.

Fuchs, Ž., and D. J. Raymond, 2007: A simple, vertically resolved model of tropical disturbances with a humidity closure. *Tellus Ser. A Dyn. Meteorol. Oceanogr.*, **59**, 344–354, https://doi.org/10.1111/j.1600-0870.2007.00230.x.

Fuchs-Stone, Ž., D. J. Raymond, and S. Sentić, 2019: A simple model of convectively coupled equatorial rossby waves. *J. Adv. Model. Earth Syst.*, **11**, 173–184, https://doi.org/10.1029/2018ms001433.

Gonzalez, A. O., and X. Jiang, 2019: Distinct propagation characteristics of intraseasonal variability over the tropical west pacific. *J. Geophys. Res.*, **124**, 5332–5351, https://doi.org/10.1029/2018jd029884.

Grabowski, W. W., and M. W. Moncrieff, 2004: Moisture–convection feedback in the tropics. *Quart. J. Roy. Meteor. Soc.*, **130**, 3081–3104, https://doi.org/10.1256/qj.03.135.

Hayashi, Y., 1970: A theory of large-scale equatorial waves generated by condensation heat and accelerating. *Journal of the Meteorological Society of Japan. Ser. II*, **48**, 140–160.

——, 1971: A generalized method of resolving disturbances into progressive and retrogressive waves by space Fourier and time cross-spectral analyses. *Journal of the Meteorological Society of Japan. Ser. II*, **49**, 125–128.

Henderson, D. S., T. L'Ecuyer, G. Stephens, P. Partain, and M. Sekiguchi, 2013: A multisensor perspective on the radiative impacts of clouds and aerosols. *J. Appl. Meteorol. Climatol.*, **52**, 853–871, https://doi.org/10.1175/jamc-d-12-025.1.

Hersbach, H., and Coauthors, 2020: The ERA5 global reanalysis. *Q. J. R. Meteorol. Soc.*, **146**, 1999–2049, https://doi.org/10.1002/qj.3803.

Hirota, N., Y. N. Takayabu, M. Watanabe, and M. Kimoto, 2011: Precipitation Reproducibility over Tropical Oceans and Its Relationship to the Double ITCZ Problem in CMIP3 and MIROC5 Climate Models. *J. Clim.*, **24**, 4859–4873, https://doi.org/10.1175/2011JCLI4156.1.

Hodges, K. I., D. W. Chappell, G. J. Robinson, and G. Yang, 2000: An improved algorithm for generating global window brightness temperatures from multiple satellite infrared imagery. *J. Atmos. Ocean. Technol.*, **17**, 1296–1312, https://doi.org/10.1175/1520-0426(2000)017<1296:aiafgg>2.0.co;2.

Holloway, C. E., and D. J. Neelin, 2009: Moisture Vertical Structure, Column Water Vapor, and Tropical Deep Convection. *J. Atmos. Sci.*, **66**, 1665–1683, https://doi.org/10.1175/2008JAS2806.1.

Houze, R. A., 1977: Structure and Dynamics of a Tropical Squall–Line System. *Mon. Weather Rev.*, **105**, 1540–1567, https://doi.org/10.1175/1520-0493(1977)105<1540:SADOAT>2.0.CO;2.

——, 1982: Cloud clusters and large-scale vertical motions in the tropics. *J. Meteorol. Soc. Japan*, **60**.

——, 1989: Observed structure of mesoscale convective systems and implications for large-scale heating. *Quart. J. Roy. Meteor. Soc.*, **115**, 425–461, https://doi.org/10.1002/qj.49711548702.

Houze, R. A., Jr, 2004: Mesoscale convective systems. *Rev. Geophys.*, **42**, https://doi.org/10.1029/2004rg000150.

Huang, B., C. Liu, V. Banzon, E. Freeman, G. Graham, B. Hankins, T. Smith, and H.-M. Zhang, 2021: Improvements of the Daily Optimum Interpolation Sea Surface Temperature (DOISST) Version 2.1. *J. Clim.*, **34**, 2923–2939, https://doi.org/10.1175/JCLI-D-20-0166.1.

Iguchi, T., and R. Meneghini, 1994: Intercomparison of Single-Frequency Methods for Retrieving a Vertical Rain Profile from Airborne or Spaceborne Radar Data. *J. Atmos. Ocean. Technol.*, **11**, 1507–1516, https://doi.org/10.1175/1520-0426(1994)011<1507:IOSFMF>2.0.CO;2.

——, T. Kozu, R. Meneghini, J. Awaka, and K. Okamoto, 2000: Rain-Profiling Algorithm for the TRMM Precipitation Radar. *J. Appl. Meteorol. Climatol.*, **39**, 2038–2052, https://doi.org/10.1175/1520-0450(2001)040<2038:RPAFTT>2.0.CO;2.

Janowiak, J. E., R. J. Joyce, and Y. Yarosh, 2001: A real–time global half–hourly pixel–resolution infrared dataset and its applications. *Bull. Am. Meteorol. Soc.*, **82**, 205–217, https://doi.org/10.1175/1520-0477(2001)082<0205:artghh>2.3.co;2.

Johnson, R. H., T. M. Rickenbach, S. A. Rutledge, P. E. Ciesielski, and W. H. Schubert, 1999: Trimodal characteristics of tropical convection. *J. Clim.*, **12**, 2397–2418, https://doi.org/10.1175/1520-0442(1999)012<2397:tcotc>2.0.co;2.

Khouider, B., and A. J. Majda, 2006: A simple multicloud parameterization for convectively coupled tropical waves. Part I: Linear analysis. *J. Atmos. Sci.*, **63**, 1308–1323, https://doi.org/10.1175/jas3677.1.

——, and ——, 2007: A Simple Multicloud Parameterization for Convectively Coupled Tropical Waves. Part II: Nonlinear Simulations. *J. Atmos. Sci.*, **64**, 381–400, https://doi.org/10.1175/JAS3833.1.

——, and ——, 2008: Equatorial Convectively Coupled Waves in a Simple Multicloud Model. *J. Atmos. Sci.*, **65**, 3376–3397, https://doi.org/10.1175/2008JAS2752.1.

Kikuchi, K., and Y. N. Takayabu, 2004: The development of organized convection associated with the MJO during TOGA COARE IOP: Trimodal characteristics. *Geophys. Res. Lett.*, **31**, https://doi.org/10.1029/2004gl019601.

Kiladis, G. N., and M. Wheeler, 1995: Horizontal and vertical structure of observed tropospheric equatorial Rossby waves. *J. Geophys. Res.*, **100**, 22981, https://doi.org/10.1029/95jd02415.

——, M. C. Wheeler, P. T. Haertel, K. H. Straub, and P. E. Roundy, 2009: Convectively coupled equatorial waves. *Rev. Geophys.*, **47**, https://doi.org/10.1029/2008rg000266.

Kuang, Z., 2008: A Moisture-Stratiform Instability for Convectively Coupled Waves. *J. Atmos. Sci.*, **65**, 834–854, https://doi.org/10.1175/2007JAS2444.1.

Kumar, V. V., C. Jakob, A. Protat, P. T. May, and L. Davies, 2013: The four cumulus cloud modes and their progression during rainfall events: A C-band polarimetric radar perspective. *J. Geophys. Res.*, **118**, 8375–8389, https://doi.org/10.1002/jgrd.50640.

Lau, K.-H., and N.-C. Lau, 1990: Observed Structure and Propagation Characteristics of Tropical Summertime Synoptic Scale Disturbances. *Mon. Weather Rev.*, **118**, 1888–1913, https://doi.org/10.1175/1520-0493(1990)118<1888:OSAPCO>2.0.CO;2.

L'Ecuyer, T. S., N. B. Wood, T. Haladay, G. L. Stephens, and P. W. Stackhouse Jr, 2008: Impact of clouds on atmospheric heating based on the R04 CloudSat fluxes and heating rates data set. *J. Geophys. Res.*, **113**, https://doi.org/10.1029/2008jd009951.

Liebmann, B., and H. H. Hendon, 1990: Synoptic-scale disturbances near the equator. *J. Atmos. Sci.*, **47**, 1463–1479, https://doi.org/10.1175/1520-0469(1990)047<1463:ssdnte>2.0.co;2.

Lin, J.-L., and Coauthors, 2006: Tropical Intraseasonal Variability in 14 IPCC AR4 Climate Models. Part I: Convective Signals. *Journal of Climate*, **19**, 2665–2690, https://doi.org/10.1175/jcli3735.1.

——, M.-I. Lee, D. Kim, I.-S. Kang, and D. M. W. Frierson, 2008: The Impacts of Convective Parameterization and Moisture Triggering on AGCM-Simulated Convectively Coupled Equatorial Waves. *J. Clim.*, **21**, 883–909, https://doi.org/10.1175/2007JCLI1790.1.

Lindzen, R. S., 1974: Wave-CISK in the Tropics. *J. Atmos. Sci.*, **31**, 156–179, https://doi.org/10.1175/1520-0469(1974)031<0156:WCITT>2.0.CO;2.

Liou, K.-N., 1986: Influence of Cirrus Clouds on Weather and Climate Processes: A Global Perspective. *Mon. Weather Rev.*, **114**, 1167–1199, https://doi.org/10.1175/1520-0493(1986)114<1167:IOCCOW>2.0.CO;2.

Lubis, S. W., and C. Jacobi, 2015: The modulating influence of convectively coupled equatorial waves (CCEWs) on the variability of tropical precipitation. *Int. J. Climatol.*, **35**, 1465–1483, https://doi.org/10.1002/joc.4069.

Mace, G. G., and Q. Zhang, 2014: The CloudSat radar-lidar geometrical profile product (RL-GeoProf): Updates, improvements, and selected results. *J. Geophys. Res.*, **119**, 9441–9462, https://doi.org/10.1002/2013jd021374.

——, ——, M. Vaughan, R. Marchand, G. Stephens, C. Trepte, and D. Winker, 2009: A description of hydrometeor layer occurrence statistics derived from the first year of merged Cloudsat and CALIPSO data. *J. Geophys. Res.*, **114**, https://doi.org/10.1029/2007jd009755.

Madden, R. A., and P. R. Julian, 1971: Detection of a 40–50 day oscillation in the zonal wind in the tropical pacific. *J. Atmos. Sci.*, **28**, 702–708, https://doi.org/10.1175/1520-0469(1971)028<0702:doadoi>2.0.co;2.

Mapes, B., S. Tulich, J. Lin, and P. Zuidema, 2006: The mesoscale convection life cycle: Building block or prototype for large-scale tropical waves? *Dyn. Atmos. Oceans*, **42**, 3–29, https://doi.org/10.1016/j.dynatmoce.2006.03.003.

Mapes, B. E., 2000: Convective inhibition, subgrid-scale triggering energy, and stratiform instability in a toy tropical wave model. *J. Atmos. Sci.*, **57**, 1515–1535, https://doi.org/10.1175/1520-0469(2000)057<1515:cisste>2.0.co;2.

Marchand, R., G. G. Mace, T. Ackerman, and G. Stephens, 2008: Hydrometeor Detection Using Cloudsat—An Earth-Orbiting 94-GHz Cloud Radar. *J. Atmos. Ocean. Technol.*, **25**, 519–533, https://doi.org/10.1175/2007JTECHA1006.1.

Matsuno, T., 1966: Quasi-geostrophic motions in the equatorial area. *Journal of the Meteorological Society of Japan. Ser. II*, **44**, 25–43.

Matthews, A. J., and J. Lander, 1999: Physical and numerical contributions to the structure of Kelvin wave-CISK modes in a spectral transform model. *J. Atmos. Sci.*, **56**, 4050–4058, https://doi.org/10.1175/1520-0469(1999)056<4050:panctt>2.0.co;2.

Mechem, D. B., R. A. Houze Jr, and S. S. Chen, 2002: Layer inflow into precipitating convection over the western tropical Pacific. *Quart. J. Roy. Meteor. Soc.*, **128**, 1997–2030, https://doi.org/10.1256/003590002320603502.

Meissner, T., and F. J. Wentz, 2012: The Emissivity of the Ocean Surface Between 6 and 90 GHz Over a Large Range of Wind Speeds and Earth Incidence Angles. *IEEE Trans. Geosci. Remote Sens.*, **50**, 3004–3026, https://doi.org/10.1109/TGRS.2011.2179662.

Miyakawa, T., Y. N. Takayabu, T. Nasuno, H. Miura, M. Satoh, and M. W. Moncrieff, 2012: Convective momentum transport by rainbands within a Madden–Julian oscillation in a global nonhydrostatic model with explicit deep convective processes. Part I: Methodology and general results. *J. Atmos. Sci.*, **69**, 1317–1338, https://doi.org/10.1175/jas-d-11-024.1.

Moncrieff, M. W., 1992: Organized convective systems: Archetypal dynamical models, mass and momentum flux theory, and parametrization. *Quart. J. Roy. Meteor. Soc.*, **118**, 819–850, https://doi.org/10.1002/qj.49711850703.

Neelin, D. J., and J.-Y. Yu, 1994: Modes of tropical variability under convective adjustment and the madden–Julian oscillation. Part I: Analytical theory. *J. Atmos. Sci.*, **51**, 1876–1894, https://doi.org/10.1175/1520-0469(1994)051<1876:motvuc>2.0.co;2.

Nitta, T., 1972: Energy budget of wave disturbances over the Marshall Islands during the years of 1956 and 1958. *J. Meteorol. Soc. Japan*, **50**, 71–84, https://doi.org/10.2151/jmsj1965.50.2_71.

Numaguti, A., R. Oki, K. Nakamura, K. Tsuboki, N. Misawa, T. Asai, and Y.-M. Kodama, 1995: 4-5-day-period variation and low-level dry air observed in the equatorial western pacific during the TOGA-COARE IOP. *J. Meteorol. Soc. Japan*, **73**, 267–290, https://doi.org/10.2151/jmsj1965.73.2b_267.

Peters, O., and D. J. Neelin, 2006: Critical phenomena in atmospheric precipitation. *Nat. Phys.*, **2**, 393–396, https://doi.org/10.1038/nphys314.

Raymond, D., Ž. Fuchs, S. Gjorgjievska, and S. Sessions, 2015: Balanced dynamics and convection in the tropical troposphere. *J. Adv. Model. Earth Syst.*, **7**, 1093–1116, https://doi.org/10.1002/2015ms000467.

Raymond, D. J., and Ž. Fuchs, 2007: Convectively coupled gravity and moisture modes in a simple atmospheric model. *Tellus Ser. A Dyn. Meteorol. Oceanogr.*, **59**, 627–640, https://doi.org/10.1111/j.1600-0870.2007.00268.x.

Reed, R. J., D. C. Norquist, and E. E. Recker, 1977: The Structure and Properties of African Wave Disturbances as Observed During Phase III of GATE. *Mon. Weather Rev.*, **105**, 317–333, https://doi.org/10.1175/1520-0493(1977)105<0317:TSAPOA>2.0.CO;2.

Reynolds, R. W., T. M. Smith, C. Liu, D. B. Chelton, K. S. Casey, and M. G. Schlax, 2007: Daily High-Resolution-Blended Analyses for Sea Surface Temperature. *J. Clim.*, **20**, 5473–5496, https://doi.org/10.1175/2007JCLI1824.1.

Roundy, P. E., 2012: Observed Structure of Convectively Coupled Waves as a Function of Equivalent Depth: Kelvin Waves and the Madden–Julian Oscillation. *J. Atmos. Sci.*, **69**, 2097–2106, https://doi.org/10.1175/JAS-D-12-03.1.

——, and W. M. Frank, 2004: A climatology of waves in the equatorial region. *J. Atmos. Sci.*, **61**, 2105–2132, https://doi.org/10.1175/1520-0469(2004)061<2105:acowit>2.0.co;2.

Rutledge, S. A., 1991: Middle latitude and tropical mesoscale convective systems. *Rev. Geophys.*, **29**, 88–97, https://doi.org/10.1002/rog.1991.29.s1.88.

Salby, M. L., and R. R. Garcia, 1987: Transient Response to Localized Episodic Heating in the Tropics. Part I: Excitation and Short-Time Near-Field Behavior. *J. Atmos. Sci.*, **44**, 458–498, https://doi.org/10.1175/1520-0469(1987)044<0458:TRTLEH>2.0.CO;2.

Schiro, K. A., and D. J. Neelin, 2019: Deep Convective Organization, Moisture Vertical Structure, and Convective Transition Using Deep-Inflow Mixing. *J. Atmos. Sci.*, **76**, 965–987, https://doi.org/10.1175/JAS-D-18-0122.1.

Schumacher, C., R. A. Houze, and I. Kraucunas, 2004: The Tropical Dynamical Response to Latent Heating Estimates Derived from the TRMM Precipitation Radar. *J. Atmos. Sci.*, **61**, 1341–1358, https://doi.org/10.1175/1520-0469(2004)061<1341:TTDRTL>2.0.CO;2.

Shige, S., Y. N. Takayabu, W.-K. Tao, and D. E. Johnson, 2004: Spectral Retrieval of Latent Heating Profiles from TRMM PR Data. Part I: Development of a Model-Based Algorithm. *J. Appl. Meteorol. Climatol.*, **43**, 1095–1113, https://doi.org/10.1175/1520-0450(2004)043<1095:SROLHP>2.0.CO;2.

——, ——, ——, and C.-L. Shie, 2007: Spectral Retrieval of Latent Heating Profiles from TRMM PR Data. Part II: Algorithm Improvement and Heating Estimates over Tropical Ocean Regions. *J. Appl. Meteorol. Climatol.*, **46**, 1098–1124, https://doi.org/10.1175/JAM2510.1.

——, ——, and ——, 2008: Spectral Retrieval of Latent Heating Profiles from TRMM PR Data. Part III: Estimating Apparent Moisture Sink Profiles over Tropical Oceans. *J. Appl. Meteorol. Climatol.*, **47**, 620–640, https://doi.org/10.1175/2007JAMC1738.1.

——, ——, S. Kida, W.-K. Tao, X. Zeng, C. Yokoyama, and T. L'Ecuyer, 2009: Spectral Retrieval of Latent Heating Profiles from TRMM PR Data. Part IV: Comparisons of Lookup Tables from Two- and Three-Dimensional Cloud-Resolving Model Simulations. *J. Clim.*, **22**, 5577–5594, https://doi.org/10.1175/2009JCLI2919.1.

Short, D. A., and K. Nakamura, 2010: Effect of TRMM Orbit Boost on Radar Reflectivity Distributions. *J. Atmos. Ocean. Technol.*, **27**, 1247–1254, https://doi.org/10.1175/2010JTECHA1426.1.

Sobel, A., and E. Maloney, 2012: An idealized semi-empirical framework for modeling the Madden–Julian oscillation. *J. Atmos. Sci.*, **69**, 1691–1705, https://doi.org/10.1175/jas-d-11-0118.1.

——, and ——, 2013: Moisture Modes and the Eastward Propagation of the MJO. *J. Atmos. Sci.*, **70**, 187–192, https://doi.org/10.1175/JAS-D-12-0189.1.

——, S. Wang, and D. Kim, 2014: Moist static energy budget of the MJO during DYNAMO. *J. Atmos. Sci.*, **71**, 4276–4291, https://doi.org/10.1175/jas-d-14-0052.1.

Sobel, A. H., and C. S. Bretherton, 2003: Large-scale waves interacting with deep convection in idealized mesoscale model simulations. *Tellus A*, **55**, 45–60, https://doi.org/10.1034/j.1600-0870.2003.201421.x.

——, J. Nilsson, and L. M. Polvani, 2001: The weak temperature gradient approximation and balanced tropical moisture waves. *J. Atmos. Sci.*, **58**, 3650–3665, https://doi.org/10.1175/1520-0469(2001)058<3650:twtgaa>2.0.co;2.

Stevens, B., and S. Bony, 2013: What Are Climate Models Missing? *Science*, https://doi.org/10.1126/science.1237554.

Straub, K. H., and G. N. Kiladis, 2002: Observations of a convectively coupled Kelvin wave in the Eastern pacific ITCZ. *J. Atmos. Sci.*, **59**, 30–53, https://doi.org/10.1175/1520-0469(2002)059<0030:ooacck>2.0.co;2.

——, and ——, 2003a: The observed structure of convectively coupled Kelvin waves: Comparison with simple models of coupled wave instability. *J. Atmos. Sci.*, **60**, 1655–1668, https://doi.org/10.1175/1520-0469(2003)060<1655:tosocc>2.0.co;2.

——, and ——, 2003b: Extratropical forcing of convectively coupled Kelvin waves during austral winter. *J. Atmos. Sci.*, **60**, 526–543, https://doi.org/10.1175/1520-0469(2003)060<0526:efocck>2.0.co;2.

Sugiyama, M., 2009a: The Moisture Mode in the Quasi-Equilibrium Tropical Circulation Model. Part II: Nonlinear Behavior on an Equatorial β Plane. *J. Atmos. Sci.*, **66**, 1525–1542, https://doi.org/10.1175/2008JAS2691.1.

——, 2009b: The Moisture Mode in the Quasi-Equilibrium Tropical Circulation Model. Part I: Analysis Based on the Weak Temperature Gradient Approximation. *J. Atmos. Sci.*, **66**, 1507–1523, https://doi.org/10.1175/2008JAS2690.1.

Suzuki, J., M. Fujiwara, T. Nishizawa, R. Shirooka, K. Yoneyama, M. Katsumata, I. Matsui, and N. Sugimoto, 2013: The occurrence of cirrus clouds associated with eastward propagating equatorial n = 0 inertio-gravity and Kelvin waves in November 2011 during the CINDY2011/DYNAMO campaign. *J. Geophys. Res.*, **118**, 12,941-12,947, https://doi.org/10.1002/2013jd019960.

Suzuki, T., Y. N. Takayabu, and S. Emori, 2006: Coupling mechanisms between equatorial waves and cumulus convection in an AGCM. *Dyn. Atmos. Oceans*, **42**, 81–106, https://doi.org/10.1016/j.dynatmoce.2006.02.004.

Takayabu, Y. N., 1994: Large-scale cloud disturbances associated with equatorial waves Part I: Spectral features of the cloud disturbances. *Journal of the Meteorological Society of Japan. Ser. II*, **72**, 433–449.

——, 2002: Spectral representation of rain profiles and diurnal variations observed with TRMM PR over the equatorial area. *Geophys. Res. Lett.*, **29**, https://doi.org/10.1029/2001gl014113.

——, and M. Murakami, 1991: The structure of super cloud clusters observed in 1-20 June 1986 and their relationship to easterly waves. *J. Meteorol. Soc. Japan*, **69**, 105–125, https://doi.org/10.2151/jmsj1965.69.1_105.

——, and T. Nitta, 1993: 3-5 Day-Period Disturbances Coupled with Convection over the Tropical Pacific Ocean. *Journal of the Meteorological Society of Japan. Ser. II*, **71**, 221–246, https://doi.org/10.2151/jmsj1965.71.2_221.

——, and W.-K. Tao, 2020: Latent Heating Retrievals from Satellite Observations. *Satellite Precipitation Measurement: Volume 2*, V. Levizzani, C. Kidd, D.B. Kirschbaum, C.D. Kummerow, K. Nakamura, and F.J. Turk, Eds., Springer International Publishing, 897–915.

——, K.-M. Lau, and C.-H. Sui, 1996: Observation of a Quasi-2-Day Wave during TOGA COARE. *Mon. Weather Rev.*, **124**, 1892–1913, https://doi.org/10.1175/1520-0493(1996)124<1892:OOAQDW>2.0.CO;2.

——, T. Iguchi, M. Kachi, A. Shibata, and H. Kanzawa, 1999: Abrupt termination of the 1997–98 El Niño in response to a Madden–Julian oscillation. *Nature*, **402**, 279–282, https://doi.org/10.1038/46254.

——, S. Shige, W.-K. Tao, and N. Hirota, 2010: Shallow and Deep Latent Heating Modes over Tropical Oceans Observed with TRMM PR Spectral Latent Heating Data. *J. Clim.*, **23**, 2030–2046, https://doi.org/10.1175/2009JCLI3110.1.

Tao, W.-K., 2003: Goddard Cumulus Ensemble (GCE) Model: Application for Understanding Precipitation Processes. *Cloud Systems, Hurricanes, and the Tropical Rainfall Measuring Mission (TRMM): A Tribute to Dr. Joanne Simpson*, W.-K. Tao and R. Adler, Eds., American Meteorological Society, 107–138.

——, and J. Simpson, 1993: Goddard Cumulus Ensemble Model. Part I: Model Description. *Terrestrial, Atmospheric and Oceanic Sciences*, **4**, 035, https://doi.org/10.3319/tao.1993.4.1.35(a).

Tao, W.-K., and Coauthors, 2003: Microphysics, radiation and surface processes in the Goddard Cumulus Ensemble (GCE) model. *Meteorology and Atmospheric Physics*, **82**, 97–137, https://doi.org/10.1007/s00703-001-0594-7.

Tulich, S. N., D. A. Randall, and B. E. Mapes, 2007: Vertical-Mode and Cloud Decomposition of Large-Scale Convectively Coupled Gravity Waves in a Two-Dimensional Cloud-Resolving Model. *J. Atmos. Sci.*, **64**, 1210–1229, https://doi.org/10.1175/JAS3884.1.

Wallace, J. M., and V. E. Kousky, 1968: Observational Evidence of Kelvin Waves in the Tropical Stratosphere. *J. Atmos. Sci.*, **25**, 900–907, https://doi.org/10.1175/1520-0469(1968)025<0900:OEOKWI>2.0.CO;2.

Wentz, F. J., 2013: SSM/I version-7 calibration report. *Remote Sensing Systems Tech. Rep*, **11012**, 1613–1627.

Wheeler, M., and G. N. Kiladis, 1999: Convectively coupled equatorial waves: Analysis of clouds and temperature in the wavenumber–frequency domain. *J. Atmos. Sci.*, **56**, 374–399, https://doi.org/10.1175/1520-0469(1999)056<0374:ccewao>2.0.co;2.

Wolding, B., J. Dias, G. Kiladis, F. Ahmed, S. W. Powell, E. Maloney, and M. Branson, 2020a: Interactions between Moisture and Tropical Convection. Part I: The Coevolution of Moisture and Convection. *J. Atmos. Sci.*, **77**, 1783–1799, https://doi.org/10.1175/JAS-D-19-0225.1.

——, ——, ——, E. Maloney, and M. Branson, 2020b: Interactions between Moisture and Tropical Convection. Part II: The Convective Coupling of Equatorial Waves. *J. Atmos. Sci.*, **77**, 1801–1819, https://doi.org/10.1175/JAS-D-19-0226.1.

Yamasaki, M., 1969: Large-scale disturbances in a conditionally unstable atmosphere in low latitudes. *Pap. Meteorol. Geophys.*,.

Yanai, M., and T. Maruyama, 1966: Stratospheric wave disturbances propagating over the equatorial Pacific. *Journal of the Meteorological Society of Japan. Ser. II*, **44**, 291–294.

——, and M. Murakami, 1970: A further study of tropical wave disturbances by the use of spectrum analysis. *Journal of the Meteorological Society of Japan. Ser. II*, **48**, 185–197.

——, S. Esbensen, and J.-H. Chu, 1973: Determination of Bulk Properties of Tropical Cloud Clusters from Large-Scale Heat and Moisture Budgets. *J. Atmos. Sci.*, **30**, 611–627, https://doi.org/10.1175/1520-0469(1973)030<0611:DOBPOT>2.0.CO;2.

Yang, G.-Y., B. Hoskins, and J. Slingo, 2003: Convectively coupled equatorial waves: A new methodology for identifying wave structures in observational data. *J. Atmos. Sci.*, **60**, 1637–1654, https://doi.org/10.1175/1520-0469(2003)060<1637:ccewan>2.0.co;2.

——, ——, and ——, 2007a: Convectively Coupled Equatorial Waves. Part I: Horizontal and Vertical Structures. *J. Atmos. Sci.*, **64**, 3406–3423, https://doi.org/10.1175/JAS4017.1.

——, ——, and ——, 2007b: Convectively Coupled Equatorial Waves. Part II: Propagation Characteristics. *J. Atmos. Sci.*, **64**, 3424–3437, https://doi.org/10.1175/JAS4018.1.

——, ——, and ——, 2007c: Convectively Coupled Equatorial Waves. Part III: Synthesis Structures and Their Forcing and Evolution. *J. Atmos. Sci.*, **64**, 3438–3451, https://doi.org/10.1175/JAS4019.1.

Yasunaga, K., and B. Mapes, 2012a: Differences between More Divergent and More Rotational Types of Convectively Coupled Equatorial Waves. Part I: Space–Time Spectral Analyses. *J. Atmos. Sci.*, **69**, 3–16, https://doi.org/10.1175/JAS-D-11-033.1.

——, and ——, 2012b: Differences between More Divergent and More Rotational Types of Convectively Coupled Equatorial Waves. Part II: Composite Analysis based on Space–Time Filtering. *J. Atmos. Sci.*, **69**, 17–34, https://doi.org/10.1175/JAS-D-11-034.1.

——, and ——, 2014: Differences between Faster versus Slower Components of Convectively Coupled Equatorial Waves. *J. Atmos. Sci.*, **71**, 98–111, https://doi.org/10.1175/JAS-D-13-03.1.

——, S. Yokoi, K. Inoue, and B. E. Mapes, 2019: Space–Time Spectral Analysis of the Moist Static Energy Budget Equation. *J. Clim.*, **32**, 501–529, https://doi.org/10.1175/JCLI-D-18-0334.1.

Yoneyama, K., and T. Fujitani, 1995: The behavior of dry westerly air associated with convection observed during the TOGA-COARE R/V Natsushima cruise. *J. Meteorol. Soc. Japan*, **73**, 291–304, https://doi.org/10.2151/jmsj1965.73.2b_291.

Zipser, E. J., 1977: Mesoscale and Convective–Scale Downdrafts as Distinct Components of Squall-Line Structure. *Mon. Weather Rev.*, **105**, 1568–1589, https://doi.org/10.1175/1520-0493(1977)105<1568:MACDAD>2.0.CO;2.